Monthly Notices of the ROYAL ASTRONOMICAL SOCIETY

MNRAS **526,** 1408–1427 (2023) https://doi.org/10.1093/mnras/stad2744
Advance Access publication 2023 September 12

On the impact of runaway stars on dwarf galaxies with resolved interstellar medium

Ulrich P. Steinwandel [1]★ Greg L. Bryan [1,2] Rachel S. Somerville,[1] Christopher C. Hayward [1] and Blakesley Burkhart[1,3]

[1]*Center for Computational Astrophysics, Flatiron Institute, 162 5th Avenue, New York, NY 10010, USA*
[2]*Department of Astronomy, Columbia University, 550 West 120th Street, New York, NY 10027, USA*
[3]*Department of Physics and Astronomy, Rutgers University, 136 Frelinghuysen Road, Piscataway, NJ 08854, USA*

Accepted 2023 September 7. Received 2023 September 7; in original form 2022 May 19

ABSTRACT

'Runaway stars' might play a role in driving galactic outflows and enriching the circumgalactic medium with metals. To study this effect, we carry out high-resolution dwarf galaxy simulations that include velocity 'kicks' to massive stars above eigth solar masses. We consider two scenarios, one that adopts a power law velocity distribution for kick velocities, resulting in more stars with high-velocity kicks, and a more moderate scenario with a Maxwellian velocity distribution. We explicitly resolve the multiphase interstellar medium (ISM) and include non-equilibrium cooling and chemistry. We sample individual massive stars from an IMF and follow their radiation input and SN feedback (core-collapse) channel at the end of their lifetime. In the simulations with runaway stars, we add additional (natal) velocity kicks that mimic two- and three-body interactions that cannot be fully resolved in our simulations. We find that including runaway or 'walkaway' star scenarios impacts mass, metal, momentum, and energy outflows as well as the corresponding loading factors. The effect on the mass loading factor is small, but we find an increase in the metal loading by a factor of 1.5 to 2. The momentum loading increases by a factor of 1.5–2. The energy loading increases by roughly a factor of 5 when runaway stars are included. Additionally, we find that the overall level of star formation is increased in the models that include runaway stars. We conclude that the inclusion of runaway stars could have an impact on the global star formation and subsequent outflow properties of dwarf galaxies.

Key words: methods: numerical – ISM: jets and outflows – galaxies: dwarf – galaxies: evolution – galaxies: formation – galaxies: ISM.

1 INTRODUCTION

The ΛCDM paradigm has been extremely successful at predicting and reproducing observations of structure formation on large scales. However, ever since the first attempts were made to model galaxy formation within this paradigm, it has been clear that *feedback* from massive stars, supernovae (SNe), and active black holes is critical for reproducing many of the observed properties of galaxies (e.g. Somerville & Davé 2015; Naab & Ostriker 2017, for reviews). Great progress has recently been made in developing large-scale simulations that reproduce many key observations of galaxy populations (e.g. Hirschmann et al. 2014; Vogelsberger et al. 2014; Schaye et al. 2015; Nelson et al. 2018; Pillepich et al. 2018). In addition, in the past decade, numerical simulations finally succeeded in producing thin, rotation-dominated discs with rather inefficient baryon-to-star conversion (e.g. Guedes et al. 2011; Agertz et al. 2013; Hopkins et al. 2014; Marinacci, Pakmor & Springel 2014; Hopkins et al. 2018) by explicitly modelling the stellar feedback that could successfully suppress star formation. From a numerical modelling aspect, this is a great success since these models demonstrated for the first time the need not only for supernova feedback but also for the early stellar feedback, such as photoionization or radiation pressure, to keep the baryon-to-star conversion efficiency low.

However, all of these simulations to one degree or another achieve this success by implementing somewhat ad hoc or phenomenological subgrid recipes, as they are not able to explicitly resolve many of the physical processes that drive feedback. For example, large-volume simulations typically have a spatial resolution of a few hundred parsecs or larger, and a baryonic mass resolution of $10^5 M_\odot$ or greater (see fig. 1 of Nelson et al. 2019 for a recent summary). Thus, these simulations typically do not resolve the multiphase interstellar medium (ISM) nor blastwaves from (individual) supernova explosions, among many other relevant processes. One of the biggest open questions in galaxy formation theory currently is how 'small-scale' processes (that occur below the explicit resolution of the simulation) may impact larger-scale and *global* properties of galaxies.

A new generation of simulations is achieving parsec to subparsec spatial resolution and mass resolution comparable to that of single stars. These simulations can explicitly resolve the multiphase ISM, the Sedov–Taylor phase of individual supernova explosions, and the multiphase character of outflows, and are therefore able to implement the physics of star formation and stellar feedback in a more explicit manner. Several groups have carried out such simulations for

★ E-mail: usteinwandel@flatironinstitute.org

subgalactic regions (Kim & Ostriker 2015; Walch et al. 2015; Kim, Ostriker & Raileanu 2017; Kim et al. 2020), typically representative of solar neighbourhood or Milky Way conditions. Recently, a few groups have been able to achieve this 'individual star' resolution and implement these more explicit feedback approaches within simulations of *entire dwarf galaxies* with accurate non-equilibrium heating and cooling (Hu et al. 2017; Emerick, Bryan & Mac Low 2019; Lahén et al. 2019b; Smith et al. 2021), which is a significant step forward. In this work, we leverage this relatively new capability to study a process that is unresolved in galaxy-scale simulations but may play an important role in shaping macroscopic galaxy properties: runaway stars.

Massive stars are pre-dominantly born in clusters. Theory and simulations governing star cluster evolution (e.g. Poveda, Ruiz & Allen 1967; Spitzer 1987; Banerjee, Kroupa & Oh 2012; Oh & Kroupa 2016) propose, that some fraction of massive stars can receive 'kicks' large enough to move them out of their natal clouds before exploding as SNe. These kicks can be imparted by gravitational interactions within a binary-star system (sometimes involving a third star), or when one of the stars in a binary explodes as a SN. In both cases, one of the massive stars can be accelerated above the escape velocity of the binary system (or even the star cluster itself). These unbound stars can easily travel at velocities >30 km s^{-1} and can thus travel the typical lengthscale of a GMC (a few tens of parsecs) on a time-scale of 1–2 Myr. However, we note that it is not clear yet which of the scenarios for the formation of runaway stars is favoured (see e.g. Fujii & Portegies Zwart 2011; Renzo et al. 2019). However, Dorigo Jones et al. (2020) point out that it is likely that the vast majority of runaway stars are realized in a SN-kick scenario. Additionally, it is important to point out that the fraction of runaway stars is highly uncertain (e.g. Stone 1991; Eldridge, Langer & Tout 2011; Silva & Napiwotzki 2011; Renzo et al. 2019; Drew, Monguió & Wright 2021).

It is extremely challenging to include these processes in a galaxy-scale simulation, for several reasons, but there have been attempts by several groups (e.g. Ceverino & Klypin 2009; Kimm & Cen 2014; Kim & Ostriker 2018; Andersson, Agertz & Renaud 2020). First, one would have to model the binary stellar initial mass function (IMF), which has significant uncertainties (e.g. Kroupa 1995; Malkov & Zinnecker 2001). Secondly, and perhaps more challenging, one would have to model two- and three-body interactions of single stars. Galaxy formation simulations are not well equipped to carry out orbital integration of multiple stellar systems, due to the nature of the gravity calculation, which is often performed with a tree or particle mesh. Hence, the gravity solvers of many astrophysical simulation codes operate in the limit of a *collisionless* system, while this is no longer a good description of few-body interactions in star clusters. At the cloud scale, there are attempts to circumvent this weakness (e.g. Fujii et al. 2021; Hirai, Fujii & Saitoh 2021; Grudić et al. 2022; Guszejnov et al. 2022). However, it has also been pointed out recently that there might be an issue with the underlying Schmidt-type star formation recipes often applied in galaxy-scale simulations which makes it intrinsically hard to disperse star clusters on the correct time-scales (e.g. Smith et al. 2021; Hislop et al. 2022); this problem would likely become worse when orbits are integrated using direct summation algorithms.

Why might we expect that runaway stars could have a significant effect on galaxy-scale properties? SN feedback is believed to provide the necessary mid-plane pressure to drive a galactic outflow (Kim & Ostriker 2015; Martizzi, Faucher-Giguère & Quataert 2015; Walch et al. 2015; Gatto et al. 2017; Naab & Ostriker 2017; Steinwandel et al. 2020). However, several groups have recently put forward the idea of galactic winds that are driven by cosmic rays (CRs; e.g. Girichidis et al. 2016; Buck et al. 2020; Hopkins et al. 2021a, b, c, 2022a, b; Girichidis et al. 2022). For SN feedback, the crucial condition to drive outflows is the formation of a hot volume-filling ISM phase (e.g. Naab & Ostriker 2017; Steinwandel et al. 2020). An important factor in this picture is the host environment of the SNe (e.g. Hu et al. 2016, 2017; Hu 2019; Lahén et al. 2019a, b; Gutcke et al. 2021; Smith et al. 2021; Hislop et al. 2022). SNe that explode in the cold neutral medium or the cold molecular medium are inefficient in establishing the hot phase of the ISM as cooling times are short (a few 100 yr) and the remnants remain small ($\sim$10 pc) while in the energy-conserving Sedov–Taylor phase. This makes it relatively unlikely that subsequent SNe will explode in the bubble of previous SNe, so that no efficient outflows can be launched from the cold ISM due to the formation of superbubbles (e.g. Fielding et al. 2017; Orr et al. 2022a, b). However, the situation is different in the diffuse ISM at lower densities and higher temperatures, where SN remnants occupy a larger volume fraction. Cooling times are much longer, and a hot phase is naturally established, due to the larger occupation fraction of the remnants, which makes superbubble formation and subsequent breakout much easier.

There is a limited number of physical processes that can lead to lower ambient media preceding a SN event, some of which are driven by the host star itself (see e.g. Forbes et al. 2016; Haid et al. 2016; Hu et al. 2017; Haid et al. 2018; Emerick et al. 2019; Kim, Kim & Ostriker 2019; Smith et al. 2021; Lancaster et al. 2021a, b, for an overview of main- and post-main-sequence stellar winds, photoionization, and photoelectric heating). As discussed above, runaway stars are another mechanism that could potentially allow massive stars to travel out of their dense natal gas clouds, such that the SNe potentially explode in a warmer, lower-density environment, enhancing their ability to drive large-scale outflows (e.g. Naab & Ostriker 2017).

The impact of runaway stars has recently been studied in conditions similar to the Milky Way in Kim & Ostriker (2018) and Andersson et al. (2020). However, there has been no detailed study of this issue in the context of dwarf galaxies, which is the goal of this paper. In this paper, we create 4 simulations of isolated dwarf galaxies similar to the observed Wolff-Lundmark-Moyette (WLM) system at the outer edge of the Local Group (baryon mass of 2×10^7 M$_\odot$ and dark matter mass of 2×10^{10} M$_\odot$). We use the GRIFFIN (Galaxy Realizations with the feedback from individual massive stars) model for single star formation and resolved feedback (e.g. Lahén et al. 2019a, b; Steinwandel et al. 2020; Hislop et al. 2022; Steinwandel et al. 2022). We include a subgrid treatment for runaway stars based on existing results for the runaway population from simulations and observations (e.g. Eldridge et al. 2011; Oh & Kroupa 2016). We note that our approach includes only the natal kicks, neglecting the gravitational interaction of the star with the environment over its lifetime, and therefore may represent an upper limit on the effects of including such stars in galaxy simulations.

The remainder of the paper is structured as follows: In Section 2, we introduce the code, present the GRIFFIN model for single star formation and resolved feedback and explain in detail how we incorporate runaway stars into our model. In Section 3, we discuss the results, with a specific focus on how runaway stars may alter the outflow properties of dwarf galaxy systems and impact the ISM and CGM-ISM interface. In Section 4, we discuss our results and compare them to previous simulations in the literature. In Section 5, we summarize our results.

2 NUMERICAL METHODS

In this section, we discuss the details of our numerical modelling and present the initial conditions of our simulations. The results are part of the GRIFFIN project.[1]

2.1 Simulation code

For all simulations presented, we use the Tree-SPH code P-Gadget3 (Springel 2005; Hu et al. 2014) to carry out the gravity and hydrodynamics calculations. However, we made significant improvements by updating the baseline SPH solver to incorporate the meshless finite mass (MFM) method for solving the fluid flow, following the methods discussed in Hopkins (2015) and Gaburov & Nitadori (2011) and using the MFM implementation of Steinwandel et al. (2020). MFM represents a fully consistent second-order method in space and time and we compute fluid fluxes by solving the one-dimensional Riemann problem between single fluid tracers by adopting an HLLC-Riemann solver that accounts for the appropriate reconstruction of the contact wave. The face area is defined over the smoothing-length weighted quadrature point between the single-fluid tracers (Steinwandel in preparation). The code is then coupled to the cooling and feedback network utilized in the GRIFFIN-framework (e.g. Hu et al. 2016, 2017; Hu 2019; Lahén et al. 2019a, b; Steinwandel et al. 2020; Hislop et al. 2022).

2.2 Cooling, heating, and star formation

To model the multiphase ISM, we self-consistently model the non-equilibrium formation and destruction of molecular hydrogen and CO, following the cooling and chemistry networks developed in Glover & Mac Low (2007) and Glover & Clark (2012); we also account for the self-shielding of molecular gas based on a column density computation on a HEALPix sphere. In earlier versions of our code, this was achieved by the TREECOL method. In the latest version, this is done with a HEALPix expansion using the c library CHEALPIX. The details of the cooling and chemistry network can be found in Hu et al. (2017) and Steinwandel et al. (2020).

Star formation is modeled by utilizing an IMF-sampling approach where we sample all the stars more massive than 4 $M_\odot$ (base resolution of the simulation) as single stars. The details of the method can be found in, e.g. Hu et al. (2017); we have adopted minor updates here that will be presented in greater detail in Steinwandel (in preparation).

2.3 Stellar feedback

We follow several feedback channels for the massive stars that form within the simulation, including the photoelectric heating, the UV-radiation, and the photoionizing radiation, as well as the metal enrichment from AGB and subgrid stellar winds. However, the core of the stellar feedback scheme is the resolved SN feedback mechanism developed by Hu et al. (2017) and Steinwandel et al. (2020), which allows a self-consistent build-up of the hot phase and the momentum of individual SN events in a resolved Sedov–Taylor phase (see Hu, Sternberg & van Dishoeck 2021; Hu et al. 2022). Hence, all the outflow properties in these simulations are self-consistently driven from the hot phase of the ISM without the need for any 'ad hoc' tuning of mass loading factors as adopted in lower-resolution galaxy formation simulations. Therefore, our simulations allow a detailed study of the origin and driving of large-scale galactic winds.

We include the UV radiation of single stars following the implementation of Hu et al. (2017). This implementation makes the assumption of a (locally) optically thin medium, which is a good approximation for dwarf galaxies. Hence, we can simply sum over the radiation field for each star using an inverse square law. The lifetime functions and effective surface temperatures are taken from Georgy et al. (2013). The UV luminosity is obtained from the stellar library BaSel (Lejeune, Cuisinier & Buser 1997, 1998; Westera et al. 2002) in the energy band 6–13.6 eV, which dominates the photoelectric heating rate in the ISM. We note that one single star particle can contain more than one star in this respect, as we trace the UV-radiation from all stars with masses larger than 2 $M_\odot$. However, for star particles more massive than 4 $M_\odot$, the stars fully represent single stars. We integrate the radiation contributions while walking the gravity tree. Hence, this is effectively a ray-tracing approach modulo the angular resolution of the tree. This can be straightforwardly improved in future implementations by either including higher-order moments in the tree or modifying the tree's opening angle (i.e. running a separate gravity tree for the gravity force and UV-radiation computation). (see e.g. Grond et al. 2019, for one approach to improving our method.)

We follow photoelectric heating rates from Bakes & Tielens (1994), Wolfire et al. (2003), and Bergin et al. (2004) at the rate:

$$\Gamma_{\rm pe} = 1.3 \cdot 10^{-24} \epsilon D G_{\rm eff} n \ \ {\rm erg\ s^{-1} cm^{-3}}, \tag{1}$$

with hydrogen number density n, effective attenuation radiation field $G_{\rm eff} = G_0 \exp - 1.33 \times 10^{-21} D N_{\rm H,\,tot}$, dust-to-gas ratio D, total hydrogen column density $N_{\rm H,\,tot}$ and photoelectric heating rate ϵ that can be determined via:

$$\epsilon = \frac{0.049}{1 + 0.004 \psi^{0.73}} + \frac{0.037 (T/10000)^{0.7}}{1 + 2 \cdot 10^{-4} \psi} \tag{2}$$

where ψ denotes $G_{\rm eff} \sqrt{T} / n^-$, with electron number density n^- and gas temperature T.

We include a treatment for photoionizing radiation since previous work (e.g. Hu et al. 2017; Emerick et al. 2019; Steinwandel et al. 2020; Smith et al. 2021) has revealed that photoionization feedback can have a significant impact on ISM properties and star formation rates. Ideally, we would utilize a proper radiative transfer scheme for this purpose, but this is prohibitively computationally expensive. Thus we model the photoionizing feedback locally around each photoionizing source in the simulation via a Stroemgren approximation, similar to the approach used in Hopkins, Quataert & Murray (2012) and later improved by Hu et al. (2017).

Every star particle that fulfills the criterion of having one or more constituent.[2] stars with mass $m_{\rm IMF} > 8\ M_\odot$ is treated as a photoionizing source in our simulations. Thus all of the neighbouring gas particles are labeled as photoionized within some radius R_S around the star and all of the surrounding molecular and neutral hydrogen species are destroyed and transferred to H^+ (we set the ionizing fraction to 0.9995 in our chemical model). In addition, we heat the surrounding gas within R_s to 10^4 K, which is the temperature in HII-regions, by providing the necessary energy input from the ionizing source. This procedure is straightforward if R_S is known

[1] https://wwwmpa.mpa-garching.mpg.de/~naab/griffin-project/

[2] While the algorithm samples single stars from 4 to 50 solar masses, we draw stellar masses from 0.08 to 50 solar masses. Hence, even one massive star can in principle consist of more than one constituent, e.g. if we first draw a 1-solar-mass star and then the massive star afterward.

(i.e. as long as the gas density is roughly constant). However, in practice, this will rarely be the case, and we obtain R_S iteratively, where we use the classic Stroemgren-radius as an 'educated guess'.

We include the feedback from core-collapse SNe in our simulations. The supernova feedback routines presented in this section are the core feedback mechanism in our current galaxy formation and evolution framework. Every supernova distributes 10^{51} erg into the nearest 32 neighbours. We follow metal enrichment using the yields of Chieffi & Limongi (2004), who present stellar yields for stars from zero metallicity to solar metallicity for progenitors ranging from 13 to 35 $M_\odot$, from which we interpolate our metal enrichment routines. When a star explodes in a CCSN, the mass is added to the surrounding 32 (one-kernel) gas particles with the metal mixture that is expected from the above yields. It is important to include the appropriate metal yields since the cooling rate is sensitive to the injected metal composition and, thus, to the properties of the ambient medium and thus, in the end, to the correct density and phase structure of the ISM. In this context, we note that this then depends on the details of the underlying stellar evolution itself since this could potentially affect the results of our simulations, as we do by now include a rather large subset (e.g. the far-ultraviolet field and the derived photoelectric heating rate, metal enrichment and photoionizing fluxes of single stars) of stellar evolution models in our simulations. We note this as a general caveat, as stellar evolution is still a developing field, and in our treatment, we rely upon the error bars predicted by this subfield. In the future, it would be desirable to have more interaction between experts on stellar evolution and experts on ISM and galaxy-scale simulations to tackle this problem in greater detail. As the amount of metal mass that is distributed into the neighbours of the star particle can be much larger than the mass of one gas particle, we split the gas particles after the enrichment has taken place if the mass exceeds the initial particle mass resolution of the simulation by a factor of two, to avoid numerical artifacts. The split particles inherit all the physical properties that were present in the parent particle, including specific internal energy, kinetic energy, metallicity, and chemical abundances. The particle mass is split by a factor of two and the position is offset by one-fifth of the parent particle's smoothing length in a random (isotropic) direction to avoid overlap of the two newly spawned particles. The spawning process requires a new domain decomposition and a re-build of the gravity tree, which makes the code somewhat slower.

2.4 Treatment of runaway stars

While the spatial and mass resolution of our simulation is relatively high by current standards, we are not yet capable of accurate modelling of the two-, three-, and few-body interactions needed to self-consistently account for the velocity offset from which runaway O/B stars originate. We note that attempts can be made to self-consistently model these phenomena in the near future in galaxy-scale simulations employing the methods presented in Rantala et al. (2017) and Rantala et al. (2020; higher-order symplectic), and there have been recent demonstrations of similar methods on the cloud scale for higher-order Hermite integration of star clusters (e.g. Grudić et al. 2022; Guszejnov et al. 2022). However, it is not currently possible to accurately compute the forces for two- or three-body encounters in a galaxy-scale simulation that also takes a detailed ISM model into account. A first-order approximation for the effect of runaway stars can be obtained by constructing a 'subgrid' model for the velocity kicks for the massive O/B stars that become runaway stars. In the following, we present two models, one motivated by simulations for a strong runaway case and another that represents a weaker walkaway case.

2.4.1 *The runaway case: power law velocity distribution*

In the strong runaway model, we assume that the velocity distribution follows a simple power law

$$f_{\rm vel} \propto v^{-\beta}, \tag{3}$$

where β is the velocity power law slope, which is dependent on several factors. One popular scenario for runaway star formation occurs when a binary system undergoes gravitational scattering processes with a third star. Thus it is straightforward to assume that β is mainly driven by the number of binary systems in the star cluster and the relaxation time of the star cluster itself. Moreover, in reality, star clusters can be disrupted (e.g. due to internal supernova events or tidal interactions with other star clusters) which is also important for setting β. All these processes can lead to velocity kicks following the distribution of equation (3). However, there would be a time delay that comes from the direct N-body interactions which are not captured by our approach. This is a clear limitation of applying random (isotropic) velocity kicks. To accurately model star cluster formation and evolution it is necessary to solve the direct N-body system, which would give a reliable estimate for β (Eldridge et al. 2011; Perets & Šubr 2012; Oh & Kroupa 2016; Renzo et al. 2019). In detail, the velocity distribution may depend on the mass of the star as well as on the properties of the star cluster. Alternatively, one could follow an empirically motivated approach and adopt an estimate for β directly from observations (e.g. Blaauw 1961; Gies 1987; Hoogerwerf, de Bruijne & de Zeeuw 2000, 2001; Comerón & Pasquali 2007). In our first runaway model, we will follow a theoretically motivated approach by adopting estimates from Oh & Kroupa (2016). This will allow a direct comparison to Andersson et al. (2020), who investigated the effects of runaway stars in galaxy simulations of the Milky Way.

We start our modelling by building a subgrid model for runaway stars in which we adopt a power law velocity distribution following equation (3) with slope $\beta = 1.8$. To do so, we slightly modify our IMF-sampling approach and add velocity kicks to stars that are more massive than $8M_\odot$. First, we have to sample the velocity distribution of equation (3). This can be accomplished by drawing a random number p and obtaining the absolute value of the velocity kick of particle i in the following manner:

$$v_i = v_{\rm min} \cdot (1-p)^{-\frac{1}{\beta-1}}. \tag{4}$$

We adopt a minimum value $v_{\rm min} = 3$ km s^{-1} for direct comparison with Andersson et al. (2020). We truncate the distribution at 385 km s^{-1}. However, this truncation process introduces a complication. If we draw a random number between zero and one and we calculate v_i following equation (4), then it can happen that we naturally sample values above 385 km s^{-1}. We want to truncate the sampling in order to obtain a distribution where 14 per cent of the stars obtain a velocity kick of more than 30 km s^{-1}, which is in good agreement with observations. The sampling of values above 385 km s^{-1} can be related to a certain upper limit $p_{\rm max}$ for the random number p, which is given by

$$p_{\rm max} = 1 - \left(\frac{3}{385}\right)^{\frac{4}{5}} \approx 0.9744. \tag{5}$$

We thus only accept the random number p if it is smaller than or equal to $p_{\rm max}$. This ensures that we obtain a velocity power law distribution

with a slope of $\beta = 1.8$ and a fraction of stars with velocity kicks of more than 30 km s^{-1} of 14 per cent.

2.4.2 *The walkaway case: Maxwellian velocity distribution*

The second scenario that we adopt for velocity kicks is designed to mimic the more conservative case of so-called walkaway stars, where the bulk of the stars in the velocity distribution are moving at a speed lower than 10 km s^{-1}, following a velocity distribution that is consistent with a Maxwell–Boltzmann distribution:

$$p(v) \propto v^2 \exp\left(-\frac{v^2}{2\sigma^2}\right) \tag{6}$$

where σ is the width of the distribution. This is motivated by previous work, both observational and theoretical, that shows some indication for a Maxwellian distribution (e.g. Eldridge et al. 2011; Silva & Napiwotzki 2011). However, we note that we take a rather conservative approach that is more consistent with previous research such as Renzo et al. (2019), which suggests that the bulk of runaway stars can actually be classified as walkaway stars. While such a distribution is a little harder to sample than the power law from the previous section, it becomes almost trivial when considering that the distribution of equation (6) is the three-dimensional representation of the Maxwell–Boltzmann distribution integrated over the solid angle in spherical coordinates. Hence, this distribution in Cartesian coordinates consists of three (independent) Gaussian distributions. The latter can be straightforwardly sampled by a Gaussian random number generator, which is available in the *gsl* package as the Ziggurat algorithm and is the fastest way of sampling the distribution of equation (6). We note that we explored different options to sample this distribution, such as the Box-Muller method, which can obtain Gaussian random numbers by utilizing a linear combination of four uniform random numbers. In practice, the difference is marginal, but the Ziggurat algorithm is much faster. We note that for this model, we also adopt a probability for a star to get any velocity kick. This is motivated by the fact that a fraction of stars will be born as single stars and a fraction will be born as binary stars. In this model, we assume that only binary stars can receive a velocity kick and we adopt a binary star fraction of 50 per cent[3] We note that we did not assume this in the first model, in order to have a model close to the results of Oh & Kroupa (2016) and the implementation of Andersson et al. (2020). Note that we do not explicitly sample the binary IMF, which is a clear limitation of this model. Since this model is supposed to represent the more conservative walkaway case, we adopt a relatively low value of $\sigma = 32$ km s^{-1} that leads to a fraction of stars reaching more than 30 km s^{-1} in velocity of around 8 per cent and an average stellar velocity of around 15–20 km s^{-1}.

2.5 Initial conditions and simulations

In our set of simulations, we use the initial conditions of an isolated dwarf galaxy with a baryon mass of 2×10^7 M$_\odot$ and a dark matter mass of 2×10^{10} M$_\odot$, which is an analog of a classic WLM system. The mass resolution is set to 4 M$_\odot$. The force softening for this system is 0.1 pc. While our choice for gravitational softening is rather aggressive, we note that extensive testing of different values of this parameter indicates that the choice has little effect on global galactic properties such as morphology, star formation, and outflow rates. However, we note that a softening length of less than 0.1 leads to suboptimal gravity time-stepping behaviour due to runaway star formation in dense regions that results in the gravitational ejection of single stars to arbitrarily large velocities. This effect is mainly significant in runs without PI-radiation (not presented here). The softening is roughly comparable to the size of the kernel that we observe in the dense regions of the ISM during the simulation. The initial conditions are generated with the code presented in Springel, Di Matteo & Hernquist (2005), often referred to as 'MakeDiscGal' or 'Makegalaxy'.

In total, we carry out four simulations: *WLM-fiducial*, *WLM-RunP* (power law runaway stars), *WLM-RunM* (Maxwellian runaways), and *WLM-inplane* (runaways only in the x-y plane), summarized in Table 1. The first case, *WLM-fiducial*, represents a baseline case without runaway stars. The second case, *WLM-RunP*, represents a strong runaway case. The third case, *WLM-RunM*, represents a weaker runaway scenario, in which stars do not receive such high velocity kicks as in the *WLM-RunP* scenario. The final case, *WLM-inplane*, samples the same power-law velocity distribution as *WLM-RunP*, but kicks are only imparted in the x-y plane. This allows us to test the impact of runaways migrating within the plane of the galaxy versus escaping above or below the disc.

2.6 Definitions for outflow rates, inflow rates, loading factors, and metal enrichment factors

We follow the definitions for outflow rate, inflow rate, mass loading, and enrichment factors of previous work – specifically, the definitions presented in Hu (2019). Generally, galactic wind quantities can be split into mass-flux (m), momentum-flux (p), and energy-flux (e), defined as:

$$\mathcal{F}_\mathrm{m} = \rho \mathbf{v}, \tag{7}$$

$$\mathcal{F}_\mathrm{p} = \rho \mathbf{v} \cdot \mathbf{v} + P, \tag{8}$$

$$\mathcal{F}_\mathrm{e} = (\rho e_\mathrm{tot} + P)\mathbf{v}, \tag{9}$$

with ρ, v, and P given as the fundamental fluid variables density, velocity, and pressure, respectively. At all times, e_tot is defined as the total energy per unit mass $e_\mathrm{tot} = 0.5 \times \mathbf{v}^2 + u$, where u is the internal energy per unit mass. In standard code units, u takes the units kms^{-2}. We note this to avoid confusion with converting these units to proper cgs units in the sections below.

In this work, if not stated otherwise, all the flow rates are measured at a height of 1 kpc above the mid-plane of the galaxies in a plane-parallel patch with thickness dr, where $dr = 0.1$ kpc.

We will adopt the following definitions for inflow and outflow rates, with the total flow rates defined as $\dot{M} = \dot{M}_\mathrm{out} - \dot{M}_\mathrm{in}$, $\dot{p} = \dot{p}_\mathrm{out} - \dot{p}_\mathrm{in}$ and $\dot{E} = \dot{E}_\mathrm{out} - \dot{E}_\mathrm{in}$. Outflow is defined by a positive value of the radial velocity given by $\mathbf{v} \cdot \hat{\mathbf{n}} = v_r > 0$, and inflow is defined as the material in the patch with negative radial velocity $v_r < 0$. Hence, we can write down the discrete inflow and outflow rates for mass, momentum, and energy:

$$\dot{M}_\mathrm{out} = \sum_{i, v_{i,r} > 0} \frac{m_i v_{i,r}}{dr}, \tag{10}$$

$$\dot{M}_\mathrm{in} = -\sum_{i, v_{i,r} < 0} \frac{m_i v_{i,r}}{dr}, \tag{11}$$

$$\dot{p}_\mathrm{out} = \sum_{i, v_{i,r} > 0} \frac{m_i [v_{i,r}^2 + (\gamma - 1) u_i]}{dr}, \tag{12}$$

[3]The choice of 50 per cent is rather ad hoc since most of the exact fraction of runaway/walkaway stars is not exact.

Table 1. Overview of the physics variations adopted in our different simulations. For convenience, we follow similar naming conventions as those adopted in Hu et al. (2017).

Name	Core-collapse SNe	Photoionizing radiation	Photoelectric heating	Runaway stars
WLM-fiducial	✓	✓	✓	x
WLM-RunP	✓	✓	✓	power law distribution
WLM-RunM	✓	✓	✓	Maxwellian distribution
WLM-inplane	✓	✓	✓	Maxwellian (sampling only for v_x and v_y)

$$\dot{p}_{\rm in} = -\sum_{i,v_{i,r}<0} \frac{m_i[v_{i,r}^2 + (\gamma-1)u_i]}{dr}, \quad (13)$$

$$\dot{E}_{\rm out} = \sum_{i,v_{i,r}>0} \frac{m_i[v_i^2 + \gamma u_i]v_{i,r}}{dr}, \quad (14)$$

$$\dot{E}_{\rm in} = -\sum_{i,v_{i,r}<0} \frac{m_i[v_i^2 + \gamma u_i]v_{i,r}}{dr}, \quad (15)$$

where we use $P = \rho u(\gamma - 1)$ as an equation of state. Furthermore, we will compute metal outflow rates via:

$$\dot{M}_{\rm out} = \sum_{i,v_{i,r}>0} \frac{Z_i m_i v_{i,r}}{dr}, \quad (16)$$

$$\dot{M}_{\rm in} = -\sum_{i,v_{i,r}<0} \frac{Z_i m_i v_{i,r}}{dr}, \quad (17)$$

where Z_i is the metallicity of particle i. It is useful to investigate these parameters normalized to a set of reference quantities, defined as the so-called loading factors for mass ($\eta_{\rm m}$), metals ($\eta_{\rm Z}$), momentum ($\eta_{\rm p}$) and energy ($\eta_{\rm e}$) and given by:

(i) outflow mass loading factor: $\eta_{\rm m}^{\rm out} = \dot{M}_{\rm out}/\overline{\rm SFR}$,
(ii) inflow mass loading factor: $\eta_{\rm m}^{\rm in} = \dot{M}_{\rm in}/\overline{\rm SFR}$,
(iii) momentum outflow loading factor: $\eta_{\rm p}^{\rm out} = \dot{p}_{\rm out}/(p_{\rm SN}R_{\rm SN})$,
(iv) momentum inflow loading factor: $\eta_{\rm p}^{\rm in} = \dot{p}_{\rm in}/(p_{\rm SN}R_{\rm SN})$,
(v) energy outflow loading factor: $\eta_{\rm e}^{\rm out} = \dot{E}_{\rm out}/(E_{\rm SN}R_{\rm SN})$,
(vi) energy inflow loading factor: $\eta_{\rm e}^{\rm in} = \dot{E}_{\rm in}/(E_{\rm SN}R_{\rm SN})$,
(vii) outflow metal loading factor: $\eta_{\rm Z}^{\rm out} = \dot{M}_{\rm Z,out}/(m_{\rm Z}R_{\rm SN})$,
(viii) inflow metal loading factor: $\eta_{\rm Z}^{\rm in} = \dot{M}_{\rm Z,in}/(m_{\rm Z}R_{\rm SN})$,

where we adopt $E_{\rm SN} = 10^{51}$ erg, $p_{SN} = 3 \times 10^4$ M$_\odot$ km s^{-1}, the supernova rate $R_{SN} = \overline{\rm SFR}/(100{\rm M}_\odot)$ and the metal mass (IMF-averaged) $m_{\rm Z} = 2.5{\rm M}_\odot$, which we take for best comparison with previous dwarf galaxy studies from Hu (2019). We compute the mean star formation rate $\overline{\rm SFR}$ over the time span of one Gyr, which is the total run time of the simulation. Additionally, we define metal enrichment factors that not only quantify the amount of metal transported in the outflows but can quantify the degree to which metals are over or underabundant in galaxy outflows relative to the ISM. This can be achieved by normalizing the metal outflow rate to the mass outflow rate, weighted by the background metallicity of the galactic ISM, $Z_{\rm gal} = 0.1Z_\odot$:

(i) outflow enrichment factor: $y_{\rm Z}^{\rm out} = \dot{M}_{\rm Z,out}/(\dot{M}_{\rm out}Z_{\rm gal})$,
(ii) inflow enrichment factor: $y_{\rm Z}^{\rm in} = \dot{M}_{\rm Z,out}/(\dot{M}_{\rm in}Z_{\rm gal})$.

3 RESULTS

In this section, we will study the outflow properties of all of our dwarf galaxy simulations, with a specific focus on the time evolution of the outflow rates and wind loading factors.

3.1 Morphology

We start the discussion of our results with a brief comparison of the morphological structure of the resolved ISM in the simulations *with* and *without* runaway stars. As summarized in Table 1, the models *WLM-RunP, WLM-RunM*, and *WLM-inplane* include a numerical treatment for runaway stars, while the simulation *WLM-fiducial* is a control run that includes the feedback from massive stars (SNe, photoionization, and photoelectric heating), as described in Section 2.

In Fig. 1, we show face-on projections of the stellar surface density (left), the gas surface density (centre), and the thermal pressure (right) for the runs *WLM-fiducial* (first row), *WLM-RunP* (second row), *WLM-RunM* (third row) and *WLM-inplane* (fourth row). Qualitatively, the runs look very similar and there are only marginal differences in the global evolution of the stellar and ISM structures of the simulated systems. This trend is generally true over the full duration of the simulation. In the simulations that account for runaway stars, the stellar structure appears to be less clustered than in the cases without runaway stars, and the regular stellar tails that are clearly visible in the run *WLM-fiducial* appear to be less prominent in the simulations *WLM-RunP*, *WLM-RunM*, and *WLM-inplane*. However, the effect is marginal.

In Fig. 2, we show the same results for the simulations *WLM-fiducial* (first row), *WLM-RunP* (second row), *WLM-RunM* (third row), and *WLM-inplane* (fourth row) from the edge-on perspective. One can easily identify the thin stellar disc. Again, we note that the overall morphology is similar in all four cases. Hence, we note that the runaway stars have a minor impact on the morphological structure of the stars and the turbulent, supernova-driven ISM, relative to the variations expected just due to the stochastic nature of the underlying star formation and feedback prescription.

3.2 Star formation rate

In the top panel of Fig. 3, we show the time evolution of the star formation rate (SFR) for all four simulations: *WLM-fiducial* (black), *WLM-RunP* (blue), *WLM-RunM*, and *WLM-inplane* (orange). As in similar simulations of the WLM system in previous work, the SFR in our fiducial run is settling at around 2×10^{-4} M$_\odot$ yr^{-1}; we note that the star formation rate drops by roughly a factor of two due to the presence of photoionizing radiation, compared to runs that only include the feedback from SNe alone (e.g. Hu et al. 2017; Smith et al. 2021). Generally, the star formation rate in the two runaway models *WLM-RunP* and *WLM-RunM* do not differ significantly from the star formation rate in the fiducial run *WLM-fiducial* and in the run *WLM-inplane*, in which we only consider velocity kicks in the x and y directions, with the Maxwellian velocity kick model. However, there are some differences that we would like to point out in greater detail. First, there is a difference in the strong runaway model *WLM-RunP* compared to the other three runs, namely the height of the peaks in SFR, which can be larger by more than a factor of two for specific

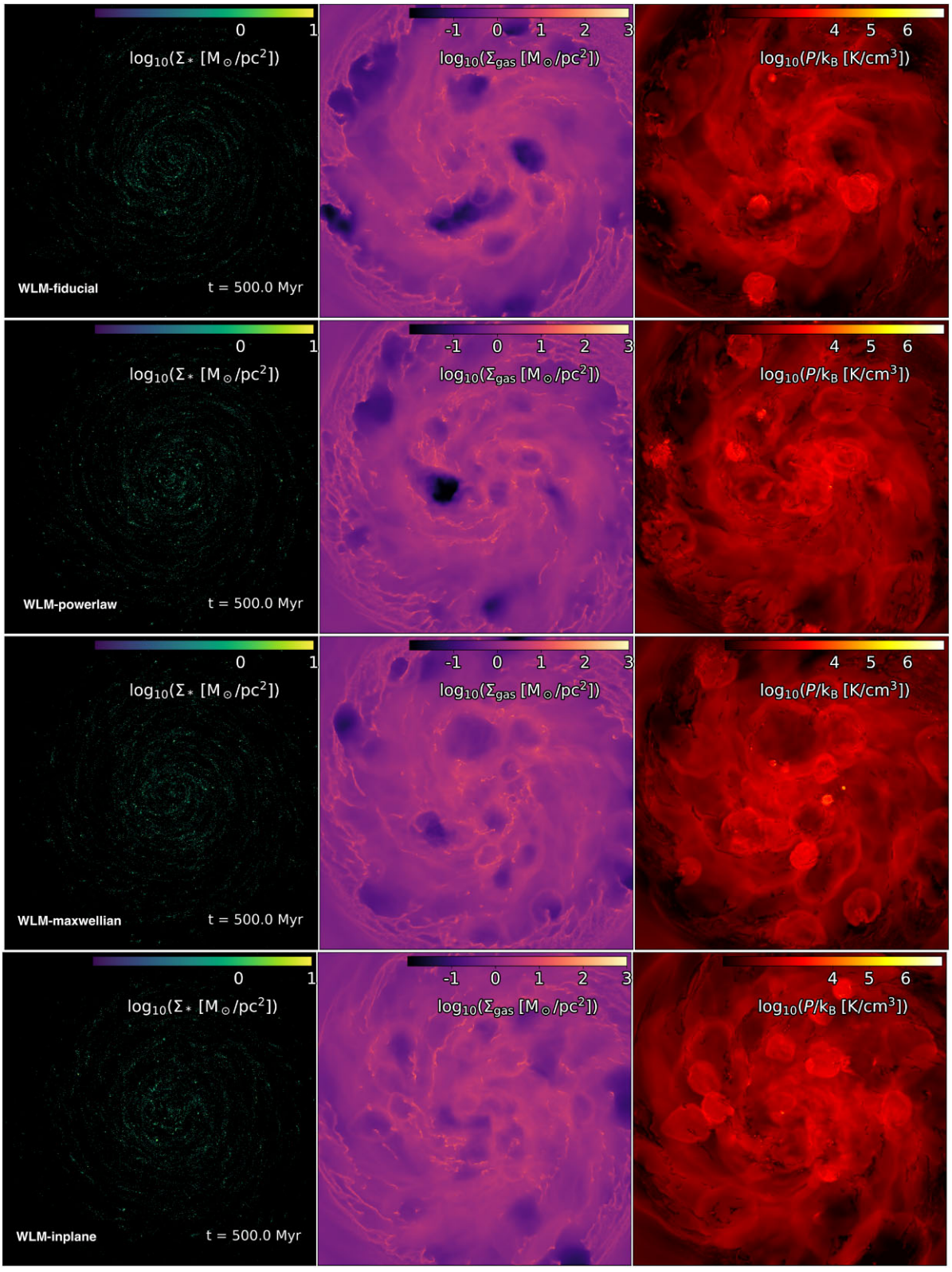

Figure 1. Visualization of the face-on stellar surface density (left), the gas surface density (centre) and the pressure (right) for our isolated dwarf galaxy simulations, for the runs *WLM-fiducial* (first row), *WLM-RunP* (second row), *WLM-RunM* (third row), and *WLM-inplane* (fourth row). We find only very minor differences between the different runs in terms of the morphology of the stellar structure and the ISM.

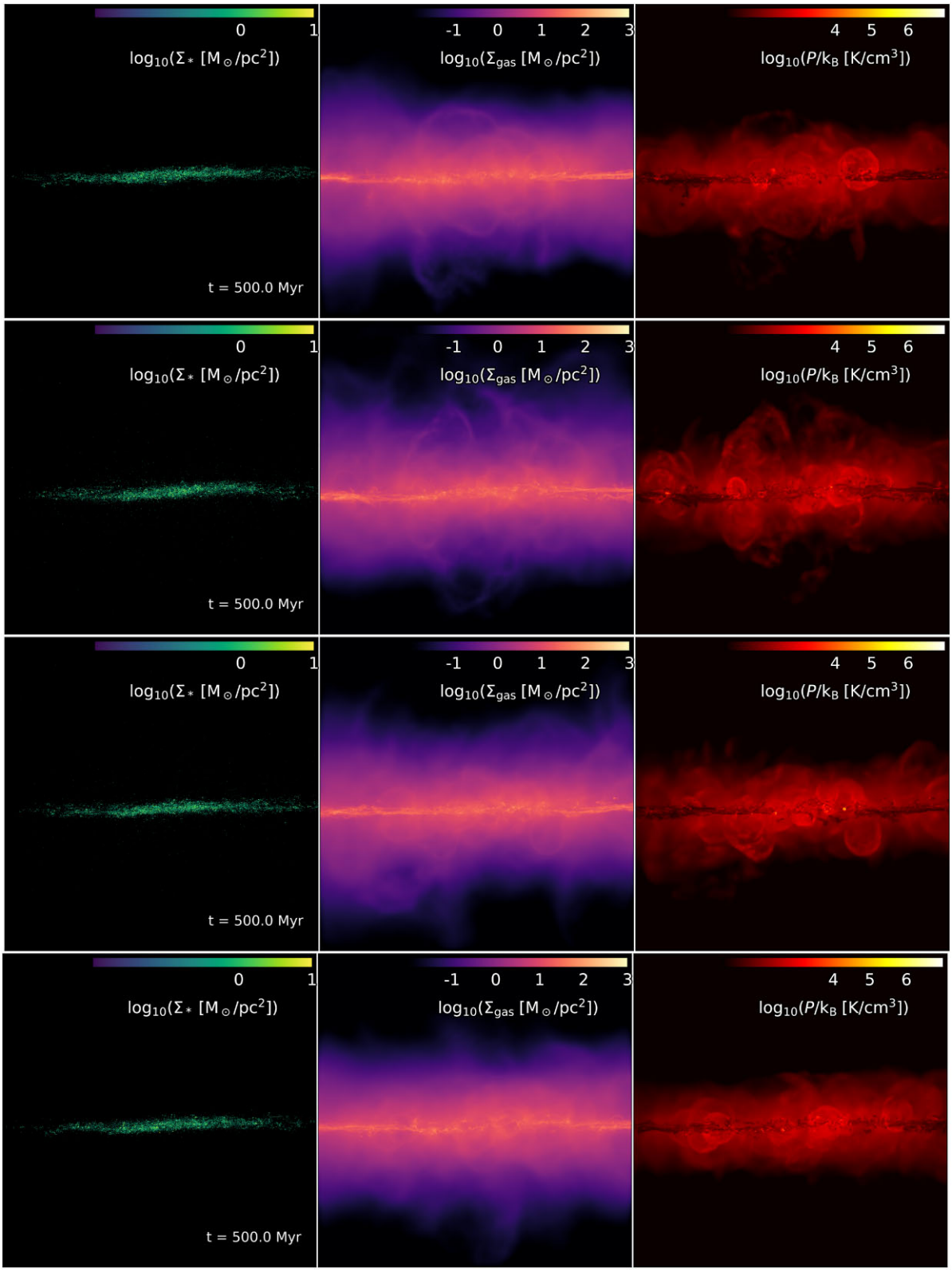

Figure 2. Visualization of the edge-on stellar surface density (left), the gas surface density (centre) and the temperature (right) for our isolated dwarf galaxy simulations, for the runs *WLM-fiducial* (first row), *WLM-RunP* (second row), *WLM-RunM* (third row), and *WLM-inplane* (fourth row). We find only very minor differences between the different runs in terms of the morphology of the stellar structure and the ISM. However, the stellar disc seems to be slightly 'puffed up' in the runs *WLM-RunP* and *WLM-RunM* compared to the runs *WLM-fiducial* and *WLM-inplane*.

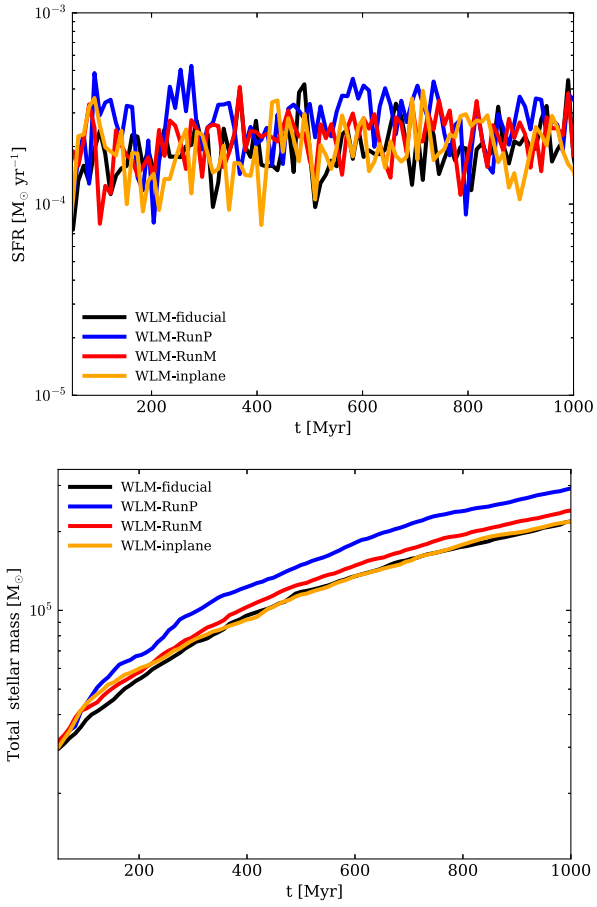

Figure 3. Star formation rate for the runs *WLM-fiducial* (black), *WLM-RunP* (blue), *WLM-RunM* (red) and *WLM-inplane* (orange) in the top panel, as well as the total stellar mass of the systems in the bottom panel as a function of time. We find a slight boost in the star formation rate in the runaway star models, which probably stems from the absence of SN feedback in the star-forming ISM due to the vertical displacement of SNe in the runs that include runaway stars.
However, the time-averaged star formation rate is only weakly influenced by this effect due to the self-regulating nature of the star formation and feedback cycle.

selected times. Thus the overall structure of the star formation history in the strong runaway model appears to be more bursty. One possible reason for this is that the velocity kicks that we apply in this particular case can easily drive some of the photoionizing sources out of the natal clouds. The other possible reason would be that the vertical repositioning of SNe removes feedback from the star-forming ISM. We discuss the details of this in Section 4.1. Since the molecular clouds in our WLM analogs are rather small (a few times 10^3 M$_\odot$ up to around a maximum of 10^4 M$_\odot$) they are easily dispersed by the effect of photoionization. However, if a large fraction of massive stars are quickly removed from their natal clouds, PI-radiation will not be able to locally quench star formation as strongly as in the reference run *WLM-fiducial*. However, since the prescription for PI-radiation acts instantaneously, the more likely explanation is that there are fewer SNe going off in the star-forming phase of the ISM and the overall star formation rate increases, which in turn can contribute to boosted outflows.

In the bottom panel of Fig. 3, we show the integrated star formation rate for all four runs, adopting the same colour scheme as for the lines.

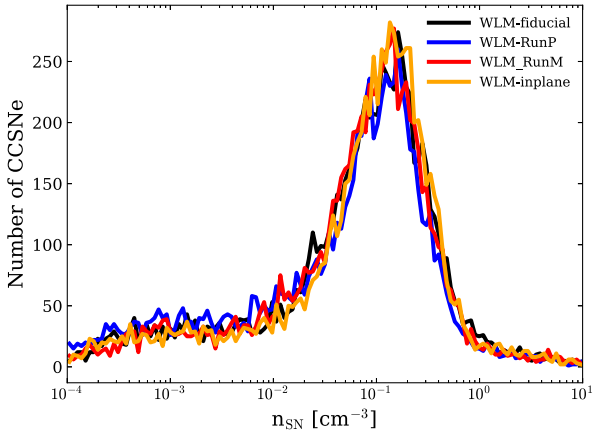

Figure 4. Distribution of the density of the gas in which SNe explode, for all runs: *WLM-fiducial* (black), *WLM-RunP* (blue), *WLM-RunM* (red), and *WLM-inplane* (orange). For all runs, we took a statistically large enough sample of 3000 SN explosions to allow direct comparison. The data are binned in 128 equally spaced logarithmic bins in the range from 10^{-4} to 10^1 cm^{-3}. Runaway stars have only a weak effect on the distribution function, but in the run *WLM-RunP*, there is a slight excess of stars exploding in lower-density environments. However, this is within the model scatter, which implies that major changes in global properties are driven by the altitude above or below the disc at which the SNe explode and not the redistribution of the SNe in the galactic plane.

While the build-up of the total stellar mass of the system is similar, the final masses (at t = 1 Gyr) are slightly different between the runs and we can see that the overall star formation rate in the runs *WLM-RunP* and *WLM-RunM* are higher by 50 and 20 per cent, respectively, compared to the *WLM-fiducial* run, indicating that runaway stars can have a significant impact on the overall star formation rate of dwarf galaxies. Generally, we find that there can be a deviation in the total mass and average star formation rate of up to a few percentage points due to model stochasticity. This can be seen by comparing the runs *WLM-fiducial* and *WLM-inplane*, where we find agreement on the per cent level. We note that we use reproducible random numbers based on Gadget's random number generator for the IMF sampling routine as well as for the sampling routine for the runaway stars' velocities; our simulations are prone to the 'butterfly effect' recently reported on in cosmological zoom simulations (e.g. Genel et al. 2019) and molecular cloud simulations (e.g. Keller et al. 2019). Hence our results are only strictly reproducible on the same machine for the same number of MPI ranks and OpenMP threads. The results of the runs *WLM-fiducial* and *WLM-inplane* are consistent with one another within the model stochasticity, but this is not the case for the runs *WLM-RunP* and *WLM-RunM*, which both show a marginal boost in the integrated star formation history. In that context, it is interesting to point out that the convergence between the models *WLM-fiducial* and *WLM-inplane* indicates that the vertical displacement of massive stars has to be responsible for the increase in overall star formation, as SNe in the dense ISM are believed to be the main regulator of a galaxy's star formation rate. The fact that the star formation rate is increasing in the runaway models will have important implications for the outflow properties in the remainder of the paper; this will be discussed in great detail in Section 4.1.

In Fig. 4, we show the supernova environmental density for all four runs, ranging from a density of 10^{-4} cm^{-3} to 10^1 cm^{-3}. The environmental density is computed in an SPH-like fashion as a

kernel-weighted sum over all the neighbours of a star particle that is flagged as experiencing a SN. The sum is computed before the ejecta is distributed. For all runs, we plot a total of ∼3000[4] SN explosions. However, due to the slight differences in the models, there is a roughly 50-Myr range in the times at which the simulations reach that value, i.e. these distributions are not plotted at the exact same time. The distribution of the environmental density of core-collapse supernova explosions is very similar between the different runs. There appears to be a slight increase in the number of SN explosions in low-density environments in the model *WLM-RunP* compared to the other three models. Furthermore, it is interesting to point out that the distribution of densities for the run *WLM-inplane* is very similar to the other models. This fact, in combination with the fact that the integrated star formation history in the models *WLM-fiducial* and *WLM-inplane* is unchanged while the integrated star formation history of the runaway models is increased, implies that the vertical displacement of SN explosions plays a key role in the observed effects on the outflow rates and loading factors. We will discuss the importance of the increase in star formation rate in the runaway models, along with the importance of SNe at high altitude, in greater detail in Section 4.1.

3.3 Phase structure and volume filling fraction

Next, we investigate the changes in the density-temperature phase space and the hot volume filling fraction of the gas. In Fig. 5, we show the time-averaged density-temperature phase space diagrams over a time span of 500 Myr from 250 to 750 Myrs, in a cylinder with radius 5 kpc and up to a height of 1 kpc (which is equivalent to 500 snapshots and around 5×10^9 particles), for the models *WLM-fiducial* (top), *WLM-RunP* (centre) and *WLM-RunM* (bottom). A more continuously populated hot phase can be seen in both runaway models. Additionally, we note that in both runaway cases, there is significantly more mass in the diffuse hot phase around 10^5 K. Gas in HII regions is clearly apparent as a horizontal line at 10^4 K.

In Fig. 6, we show the same phase diagrams, also averaged over 500 Myrs, in a volume-weighted fashion (we actually weight by effective cell size, which is $V^{1/3}$), which clearly reveals the volume-filling nature of the hot phase of the ISM.

In Fig. 7, we show the time evolution of the hot volume filling fraction for all models as a function of time. To define the hot phase, we choose a cut of 3×10^4 K, which has two motivations. The first is numerical, as this is the temperature at which we transit from a non-equilibrium cooling prescription to an equilibrium cooling prescription. The second is to be comparable with previous results of Hu et al. (2017). However, we note that this differs from the definition of the hot phase in Steinwandel et al. (2020). We compute the hot volume filling factor as the total of the volume stored in the hot phase above 3×10^4, divided by the total volume of the simulation. The volume is computed as:

$$V = \frac{4}{3}\pi h_i^3, \tag{18}$$

where h_i is the smoothing length of particle i. Alternatively, one can compute the volume as m_i/ρ_i. We tested both methods and note that there is only a minor difference between the two, which typically remains below the few percentage point level.

We can see from Fig. 7 that the volume filling fraction of hot gas in the *WLM-RunP* (strong runaway) model is significantly higher than in the other models. The weaker runaway model *WLM-RunM* has a slightly higher hot gas volume filling fraction than the *WLM-fiducial* and *WLM-inplane* models, especially at late times. We note that the exact value for the hot phase filling fraction is very sensitive to the exact value of the temperature cut, and can change by a factor of five

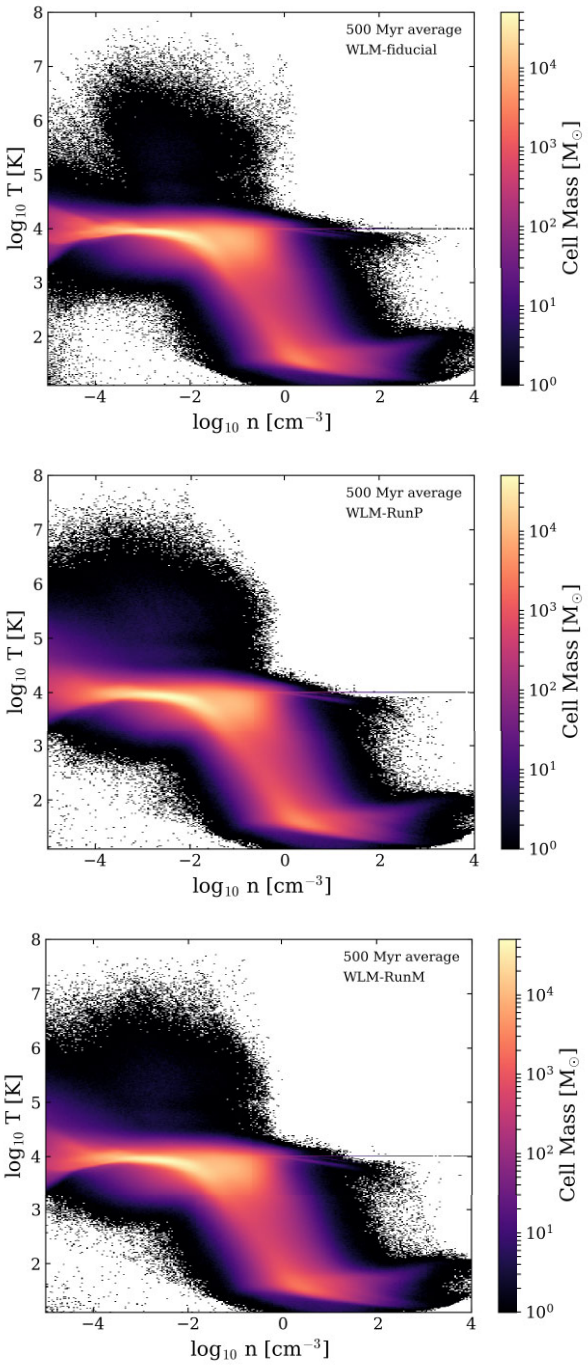

Figure 5. Time-averaged mass-weighted density-temperature phase space for the runs *WLM-fiducial* (top), *WLM-RunP* (centre), and *WLM-RunM* (bottom). All plots are averaged over a time-scale of 500 Myr. The runs *WLM-RunP* and *WLM-RunM* show an excess mass in the hot phase of the ISM. However, since the hot phase typically does not contain most of the mass, the trend is more apparent in the volume-weighted version of this figure (Fig. 6).

[4]We actually plot all SNe that went off after 1 Gyr, which is slightly more than 3000 for the runs *WLM-RunP* and *WLM-RunM*

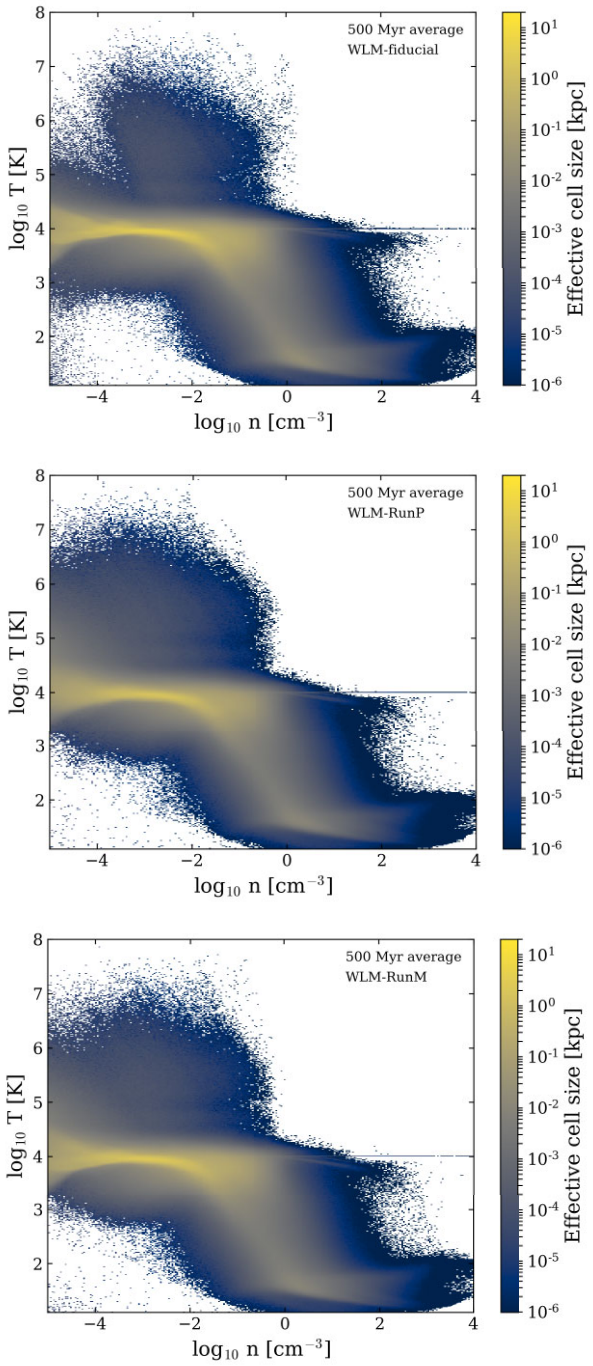

Figure 6. Time-averaged volume-weighted density-temperature phase space for the runs *WLM-fiducial* (top), *WLM-RunP* (centre) and *WLM-RunM* (bottom). All plots are averaged over a time-scale of 500 Myr. It is apparent that the inclusion of runaway stars can have a significant effect on establishing the hot, volume-filling phase of the ISM.

when the cut is varied within the range of 3×10^4 K and 3×10^5 K. Nevertheless, we find a consistently larger volume filling factor for the hot phase independent of which temperature cut we adopt.

We now turn to a quantification of the outflow properties and loading factors. In Fig. 8, we show the logarithm of the outflow velocity $u \equiv \log_{10} v_{\rm out}$ as a function of the logarithm of the sound speed $w \equiv \log_{10} c_{\rm s}$, where the colour shows the total outflow rate

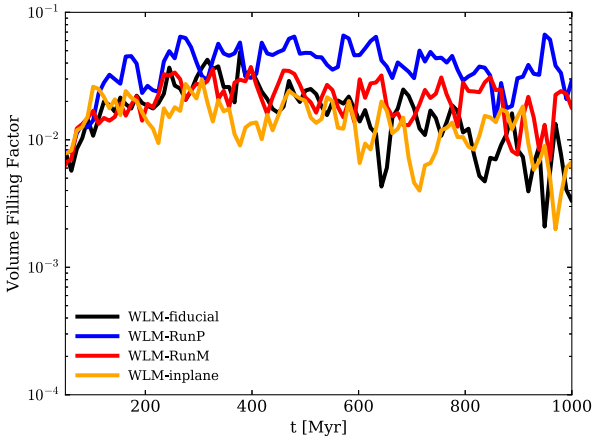

Figure 7. Volume filling factor of the hot gas (above a temperature of 3×10^4 K) as a function of time for all four models: *WLM-fiducial* (black), *WLM-RunP* (blue), *WLM-RunM* (red), and *WLM-inplane* (orange). One can clearly see that the runaway models show an increase in the volume filling factor of the hot phase. As pointed out in previous studies (Hu et al. (2017) and Steinwandel et al. (2020)), the volume filling factor is critical for driving outflows in galaxies.

in $\mathrm{M}_\odot\ \mathrm{yr}^{-1}$. The grey lines indicate surfaces of constant Bernoulli velocity given via:

$$v_{\mathcal{B}} = \left(v_{\rm out}^2 + \frac{2\gamma}{\gamma - 1} c_{\rm s}^2 \right)^{\frac{1}{2}}, \tag{19}$$

with $\gamma = 5/3$. We note that these are identical to the two-dimensional PDFs presented by Kim et al. (2020) when reduced to dimensionless units in loading factor space. Studying these diagrams for the *WLM-fiducial* (top) and *WLM-RunP* runs reveals that the bulk of the mass is transported in the cold phase. This is similar for both runs. However, the *WLM-RunP* run reveals an extended tail in a warmer, diffuse phase. This demonstrates that runaway stars have a clear impact on the phase structure of the resulting outflows in our dwarf galaxy simulation.

In Fig. 9, we show the same plots for the energy outflow rate, for *WLM-fiducial* on the top and *WLM-RunP* on the bottom, indicating that while there is a cold energy transporting phase in our dwarf galaxy simulation, there is a tail that extends to higher specific energy. This is even more true in the bottom panel for the strong runaway case *WLM-RunP*, where we find a tail that extends not only to higher sound speed but also to higher outflow velocity, which indicates that runaway stars can not only boost the mass flux but can also increase the specific energy loading as well as the total energy loading of the wind. We will discuss this in greater detail in Sections 4.1 and 4.2.

3.4 Outflow rate and outflow loading factors

We plot the main outflow diagnostics for all four simulations in Fig. 10. The top-left panel shows the mass outflow rate ($\mathrm{M}_\odot\ \mathrm{yr}^{-1}$), the top-right panel shows the metal outflow rate ($\mathrm{M}_\odot\ \mathrm{yr}^{-1}$), the bottom-left panel shows the momentum outflow rate ($\mathrm{M}_\odot\ \mathrm{km\ s}^{-1}\ \mathrm{yr}^{-1}$) and the bottom-right panel shows the energy outflow rate ($\mathrm{erg\ yr}^{-1}$). We note that the outflow rates are measured at a height of $z = 1$ kpc above the mid-plane in a patch of thickness 100 pc. We find a slight boost in the mass and the metal outflow rate by a factor of around two in the late evolutionary stages of the galactic disc when runaway stars are included. The effect is roughly the same for the strong runaway

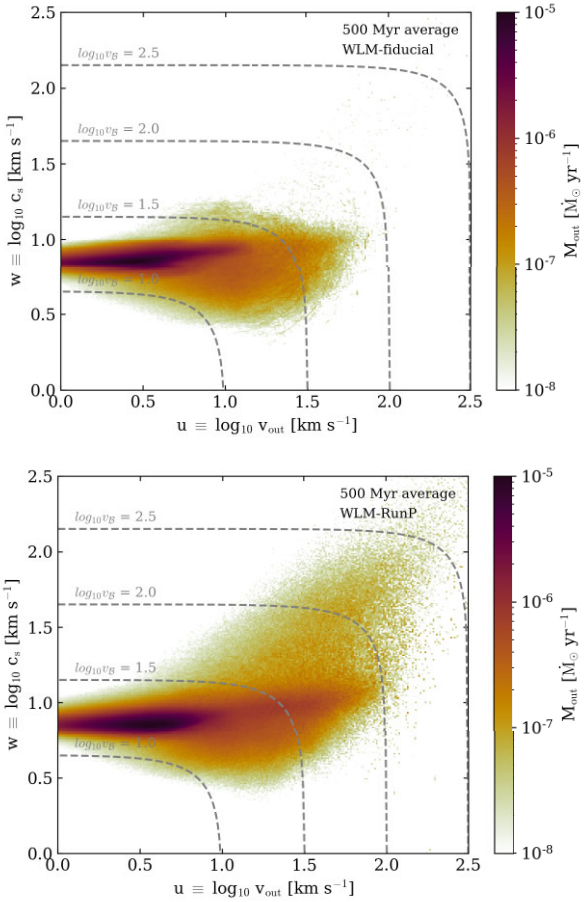

Figure 8. Outflow velocity as a function of the sound speed in logarithmic space for the models *WLM-fiducial* (top) and *WLM-RunP*. The colour code indicates the averaged outflow mass flux rate over a time span of 500 Myr. While these indicate that the bulk of the mass in the outflow is transported by the cold phase, we find a significant increase in mass transport in the hot phase of the wind, which extends to higher outflow velocities and sound speed for the simulation *WLM-RunP* (bottom). The gas selection has been made at a height of 1 kpc in a cylinder with a height of 100 pc and a radius of 5 kpc.

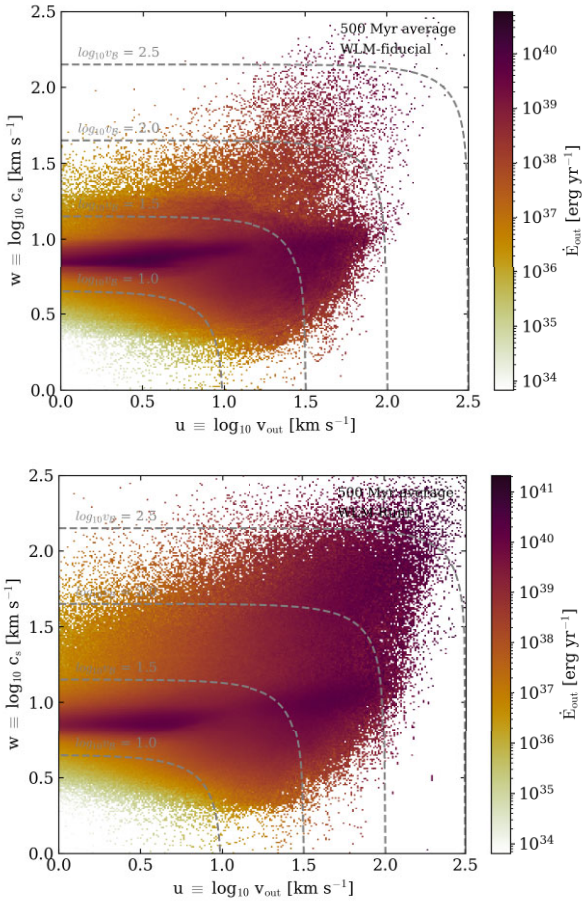

Figure 9. We show the outflow velocity as a function of the sound speed in logarithmic space for the models *WLM-fiducial* (top) and *WLM-RunP*. The colour code indicates the averaged outflow energy flux rate over a time span of 500 Myr. The energy flux carried by the phase at high velocities and high sound speeds is significantly increased when runaway stars are included in the run *WLM-RunP* (bottom).

(*WLM-RunP*) and weaker runaway (*WLM-RunM*) cases. The trend is slightly stronger for the metal outflow rate, which suggests that the runaway stars deposit their ejecta directly into the outflowing gas. While the mass and metal outflow rates are already clearly boosted in the runs with runaway stars, the effect is even stronger for the momentum and energy outflow rates. For the momentum outflow rate, we find a boost of around a factor of three, while we see a boost in the energy outflow rate by at least a factor of five and in single peaks up to a factor of around ten. Comparing the runaway runs with the reference runs *WLM-fiducial* and *WLM-inplane* indicates that this boost in energy loading is likely related to the vertical displacement of the SNe that are closer to the disc scale height of around 200 pc in our simulated system and that go off in lower density gas, as the mean travel distance of the fast-moving runaway stars is situated around a height of 200 pc. The effect is slightly suppressed in the *WLM-RunM* model, which is consistent with the scenario of walkaway stars.

In Fig. 11, we show the mass (top left), metal (top right), momentum (bottom left), and energy (bottom right) loading for all four simulations considered in this paper. While we see similar trends for the loading factors, we note that the trend in the mass loading is slightly suppressed compared to the boost we find in the mass outflow rate. The reason for this is the higher mean star formation rates in the runaway models; i.e. the star formation rate accounts for the suppression of the mass loading factors in the models with runaway stars.

3.5 Inflow rates

In Fig. 12, we show the inflow rate for mass (top left), metals (top right), momentum (bottom left), and energy (bottom right) for the simulations *WLM-fiducial* (black), *WLM-RunP* (blue), *WLM-RunM*, and *WLM-inplane* (orange). We measure the inflow rate in the same 100-pc-thick patch located at 1 kpc above/below the mid-plane. Generally, one can see that in all the models, the inflow rates decrease with time, then increase slightly after about 500 Myr. This increase is more pronounced in the models with runaway stars. In the models with runaway stars, the mass, metal, and momentum inflow rates show a similar degree of increase as the increase in outflow rates. However, the energy inflow rate decreases by only a factor of 2–3, not a factor of ∼10 as was seen in the energy outflow rate for the strong runaway model. This implies that the SN feedback energy of 'high-altitude SNe' is either efficiently kept in the CGM, due

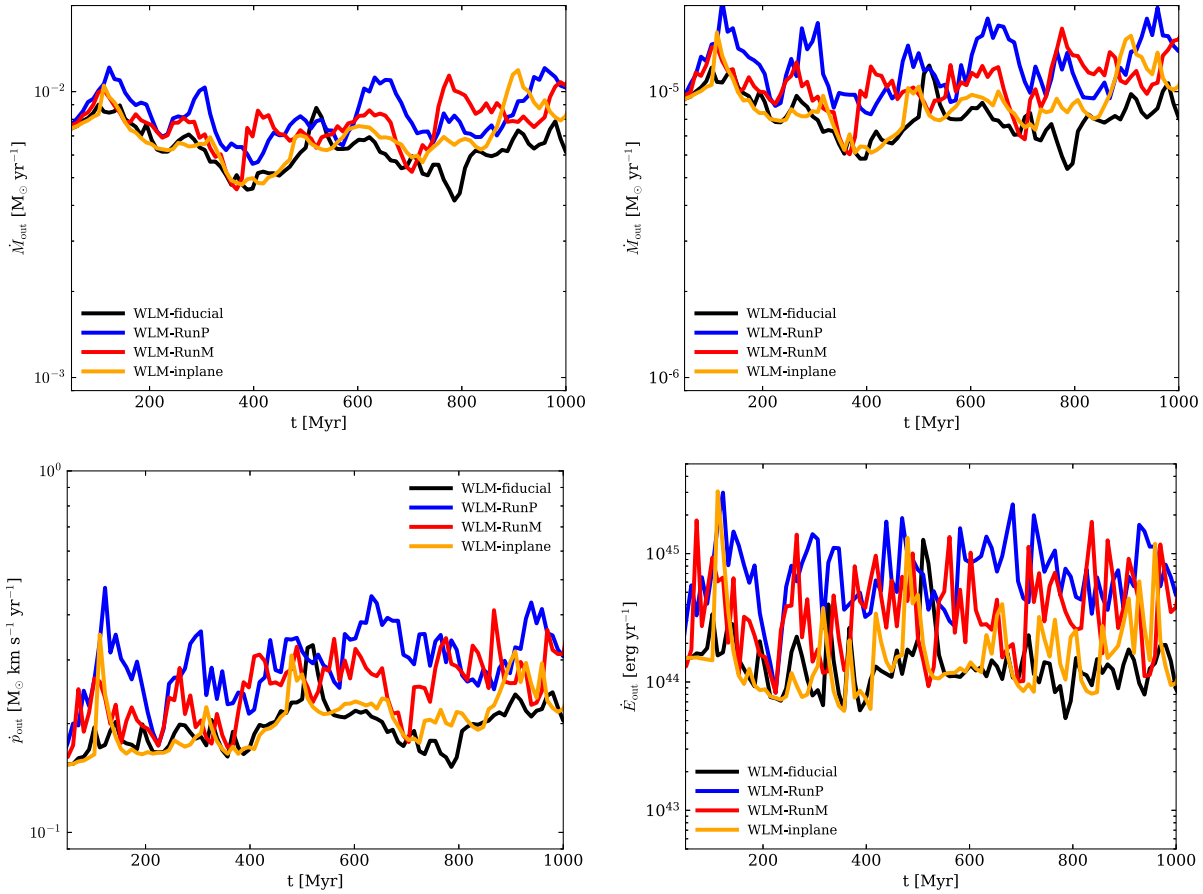

Figure 10. Mass outflow rate (top left), metal outflow rate (top right), momentum outflow rate (bottom left), and energy outflow rate (bottom right) as a function of time for all four simulated models, where black indicates the fiducial model *WLM-fiducial*, blue indicates the power law model *WLM-RunP* and red indicates the Maxwellian runaway model *WLM-RunM*. The orange line shows the runaway model *WLM-inplane*, in which we apply the velocity kicks only along the v_x and the v_y directions. The impact of runaway stars can be clearly seen in the boost of the mass, metal, and momentum outflow rates by a factor of around two (comparing blue lines to black lines). In the case of the energy outflow rate, the boost is even more significant, around a factor of seven to eight.

to mixing with lower specific energy gas, or lost to cooling in the highly metal-rich outflowing material. The latter case seems unlikely when we consider the phase structure of the mass- and volume-weighted density-temperature diagrams. These reveal more mass in the diffuse 10^5 K regime at low densities, indicating that there is a slight increase in the virial temperature of the system when runaway stars are included. We note that inflow rates are slightly larger in the runs that include a runaway/walkaway model, specifically in the last 500 Myr of evolution. This can be understood in combination with the slightly increased mass outflow rates we observe in the runaway models, which will also lead to increased inflow rates at later times. We remind the reader that most of the gas does not reach escape velocity for this dwarf galaxy (see Figs 8 and 9). The large net inflow rate at the beginning of the simulation is a remnant from our 300 Myr of SN driving before the actual simulation starts.

3.6 Metal enrichment factor

Finally, we discuss the metal outflow enrichment factor $y_Z^{\rm out}$ and the metal inflow enrichment factor $y_Z^{\rm in}$, which we show for all simulations in Fig. 13 on the top and the bottom, respectively. There is a striking increase in the metal outflow enrichment factor when runaway star modelling is included in the simulations. Generally, we find a boost of around 15–20 per cent in the metal outflow enrichment factor compared to the fiducial run and the run where we only apply the velocity kicks in the x and y directions. We note that while the metal inflow enrichment factor is also boosted compared to the reference simulations, the effect is not as strong as for the outflow enrichment factor. This indicates that runaway stars can significantly contribute to the metal enrichment of the CGM and can boost its metallicity by about 15 per cent. We discuss the impact of the higher star formation rate in the runaway models in Section 4.1. Since metals are the most important coolant in the low-density regime, this increase might have crucial consequences for mixing properties in the CGM. However, since we do not explicitly model the CGM in our simulation by including a hot cooling halo, we postpone a detailed study of CGM cooling, heating, and mixing rates, along with a detailed analysis of metal emission line properties, to future work.

4 DISCUSSION

4.1 The impact of star formation rate versus SN repositioning

There are two major findings of our study that are important for understanding galactic outflows and the specific role of runaway stars with respect to galactic outflow driving. First, we find that in

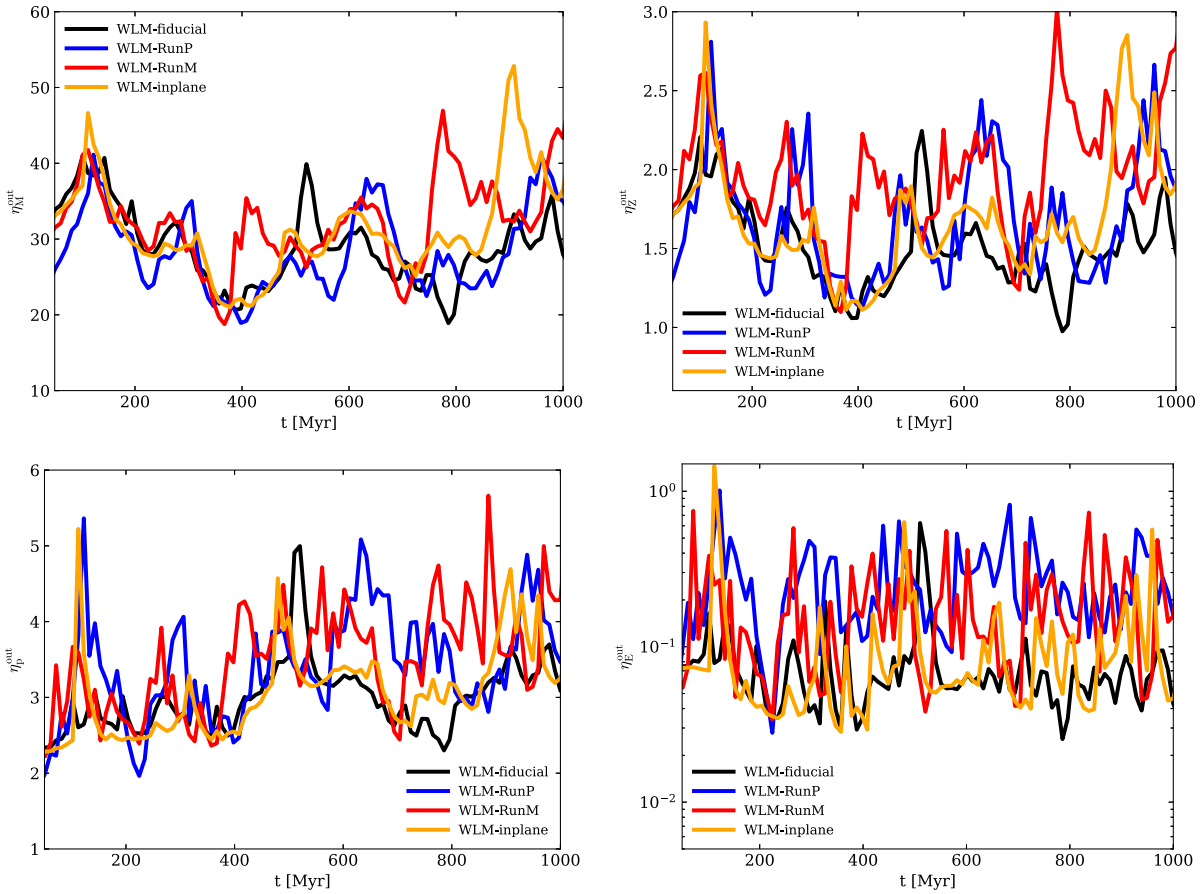

Figure 11. We show the mass outflow loading (top left), the metal outflow loading (top right), the momentum outflow loading (bottom left), and the energy outflow loading (bottom right) as a function of time for all four simulated models, where black indicates the fiducial model *WLM-fiducial*, blue indicates the power law model *WLM-RunP*, and red indicates the Maxwellian runaway model *WLM-RunM*. The orange line shows the runaway model *WLM-inplane*, in which we apply the velocity kick only along the v_x and the v_y directions. While the trend of increased mass and metal outflow rates is reduced when expressed in terms of the normalized loading factors, the trend of increased momentum and energy loading remains roughly the same as that deduced from the results of Fig. 10.

the runaway models *WLM-RunP* and *WLM-RunM*, star formation is increased. This is a 20 per cent effect for *WLM-RunM* and a 50 per cent effect for *WLM-RunP*. Additionally, we find that there is an increase in some of the outflow loading factors in the models *WLM-RunM* and *WLM-RunP*, which is especially strong for the evolution of the energy loading but is also present for the momentum and metal loading.

This raises the question of whether the changes that we observe in the outflow properties can be attributed to the increase in star formation or to the SN repositioning due to the inclusion of runaway stars. While we see from the top and bottom panels of Fig. 3 that the star formation in the models that do include runaway stars is increased, there seems to be no statistically significant evidence for changes in the SN environmental distribution that we present in Fig. 4 (although there is a slight indication for an extended low-density tail in the *WLM-RunP* model). Similarly, the phase diagrams in Figs 5 and 6 show little change except for a slight increase in the warm/hot phases in *WLM-RunM* and *WLM-RunP*. Looking more carefully, we do find an increase in the hot volume filling factor if runaway stars are included, as shown in Fig. 7, except for the model *WLM-inplane* in which we only allow in-plane velocity kicks. This closely follows the variation of SFR with the various models and so we argue that the increase in the hot volume filling factor is primarily due to the overall higher star formation rate.

In Figs 8 and 9, we presented the change in mass and energy outflow rate in time-averaged joint PDFs of sound speed and outflow velocity. These serve as a diagnostic tool for outflows, as discussed in other recent studies of galactic outflows (e.g. Fielding et al. 2017; Kim et al. 2020), and reveal that the strongest impact on the outflow structure, with or without runaway stars, is a shift from a totally warm-dominated outflow to an outflow structure that becomes more multiphase if runaway stars are included. In combination with the time evolution of the outflow rates shown in Fig. 10, they also demonstrate that the mass, metal, momentum, and energy outflow rates are all increased. Interestingly enough, this trend does not remain when we normalize by star formation rate and look at the mass loading factor itself. On the other hand, there is an increase in the metal loading factor, by a factor of 1.5 to 2, as well as the metal enrichment factor, shown in Fig. 13, which increases by roughly 20 per cent when runaway stars are included.

This means that the changes to the outflow properties are not driven by the higher star formation rate alone. This is even more apparent when considering the energy loading factor, which increases substantially (a factor of around 5) when runaway stars with vertical

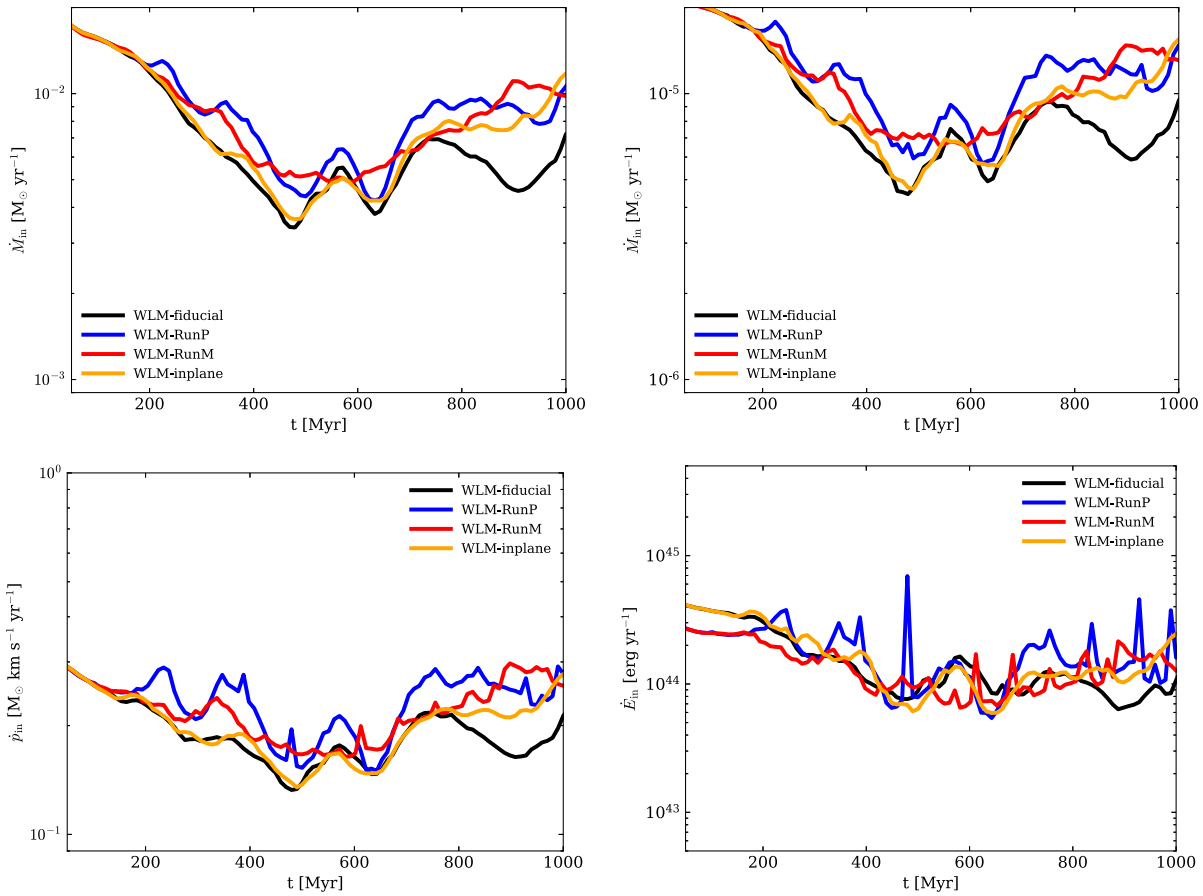

Figure 12. We show the mass inflow rate (top left), the metal inflow rate (top right), the momentum inflow rate (bottom left), and the energy inflow rate (bottom right) as a function of time for all four simulations: *WLM-fiducial* (black), *WLM-RunP* (blue), *WLM-RunM* (red), and *WLM-inplane* (orange). We find increased inflow rates for all the models that include runaway stars.

re-positioning are included, whereas there is basically no statistically relevant effect when the velocity kicks are parallel to the mid-plane.

Thus we see that, while the runaway stars do drive a higher star formation rate, the more significant change to the outflow properties (i.e. more energy and metals per supernova) is directly tied to the vertical offset of the runaway stars. This indicates that the primary effect is not that the runaway SNe explode in the low-density gas outside their natal clouds (recall that the density distribution of SN environment is almost unchanged), but the fact that they explode at altitude, which makes it easier for the remnant to blister and drive hot, metal-enriched gas out of the disc and into the halo.

4.2 Interpretation and comparison to previous work

Next, we discuss our results in the context of other studies involving isolated dwarf galaxy simulations of systems that are similar to the observed WLM system. Such simulations have been carried out by a number of different groups, with different physics implementations and different codes, generally without the inclusion of runaway stars (Hu et al. 2016, 2017; Emerick et al. 2019; Hu 2019; Gutcke et al. 2021; Smith et al. 2021; Andersson et al. 2023; Hislop et al. 2022). The closest comparisons are with the simulations by Hu et al. (2017), Hu (2019), and Smith et al. (2021), since their implemented physics modules are most similar. Additionally, the simulations of the Inferno project of Andersson et al. (2023) are very relevant for our particular study, because they include a specific treatment of runaway stars in their simulations that is very close to ours.

Hu et al. (2017) simulated the same dwarf that we did, using the Tree-SPH code P-Gadget3 based on the SPHGal (Hu et al. 2014) version of pressure-energy SPH that has been shown to perform well on shock-capturing tests and fluid-mixing instabilities, which are very important for galaxy evolution simulations. Hu et al. (2017) and Hu (2019) find values for the mass outflow rate and star formation rates that are comparable to those in our simulations. Hu et al. (2017) do not report their values for energy outflow rates, but they report the hot volume filling factor, which is around one to two per cent for their model *PE-PI-SN* but higher for their model *noPE-noPI-SN*, which only includes SNe, with values of up to 10 per cent. Generally, we find values that are in reasonable agreement with their results for the volume filling factor. We note that our model *WLM-RunP* is the one that has the highest volume filling factors for the hot phase, with values around 5 per cent, which is still lower than the values reported by Hu et al. (2017) for their SN-only case. One possibility is that at least part of the increased star formation activity is caused by the removal of photoionizing sources on the cloud scale (due to kicks). However, since our run *WLM-inplane*, which applies kicks only parallel to the mid-plane, does not show increased star formation activity, it seems more likely that the enhanced vertical deposition of SN is primarily responsible for the star formation (and hence hot VFF) increase.

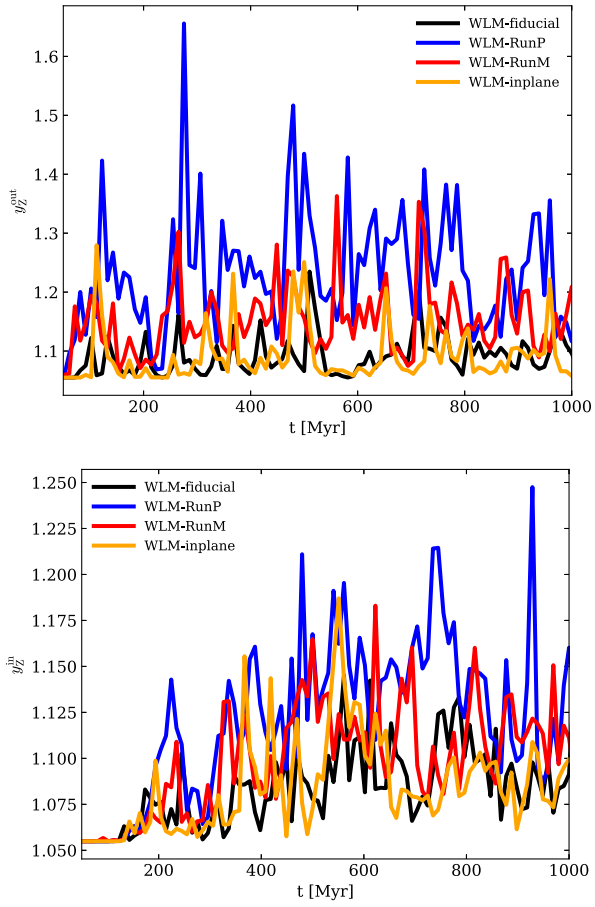

Figure 13. We show the metal outflow enrichment factor y_Z^{out} (top) and the inflow metal enrichment factor y_Z^{in} for the runs *WLM-fiducial* (black), *WLM-RunP* (blue), *WLM-RunM* (red), and *WLM-inplane* (orange). We find a significant boost in the outflow metal enrichment factor in the runs that include runaway stars. Naturally, the inflowing gas is more metal enriched as well compared to the background ISM metallicity.

Hu (2019) reports energy loading factors of around 0.1 for their simulations (almost measured at a height of 1 kpc). We note that this is about a factor of 2 higher than the values that we find for our run *WLM-fiducial*. We suggest two possible origins of this difference. First, we note that the hydrodynamics methods in our simulations and in Hu (2019) are fundamentally different. The simulations of Hu (2019) use the energy SPH method with 100 neighbours, while we use the MFM method with 32 neighbours. Recently, Hu et al. (2023a) pointed out similar findings when comparing the MFM method in Gizmo with the SPH method in Gadget, where Gizmo seems to produce energy loading factors that are significantly lower (at fixed mass loading). However, in our models that include a runaway star treatment, we find higher values that are in better agreement with the SPH results of Hu (2019). Secondly, it is worth noting that we measured in a plane-parallel slab while Hu (2019) measured in a sphere, which might change the exact value.

Smith et al. (2021) use the moving mesh code AREPO for their simulations; this adopts a second-order Riemann method on an unstaggered moving mesh and is numerically more similar to our MFM approach. The mass outflow rate that they report at 1 kpc for their *SN-PI-PE* set of simulations for the low Σ case (which they present in their appendix) is a factor of 5 to 10 lower than what we find in all our simulations, but at the same time, they find slightly higher star formation rates: a few times 10^{-4} $M_\odot$ yr^{-1}, while we find values that fluctuate around 2×10^{-4} $M_\odot$ yr^{-1}. It is worth pointing out that their simulations are a factor of 5 lower in resolution, which could potentially explain the slight increase in star formation; however, there are other factors that are more likely, such as the exact details of the numerical implementation between a fully Lagrangian particle-based method and a pseudo-Lagrangian moving mesh method (e.g. cell infection versus neighbour weighted injection in SPH/MFM). Smith et al. (2021) report mass loading factors around unity and energy loading factors between 10^{-3} and 10^{-2}, which is lower than what we find in our simulations. However, the simulations of Smith et al. (2021) are in rough agreement with the simulations of Gutcke et al. (2021) who also find values for the energy loading between 10^{-3} and 10^{-2}.

Moreover, we want to briefly comment on the disparity that is generally reported in terms of the energy loading even if a direct one-to-one comparison between codes and initial conditions is carried out, such as in the recent work of Hu et al. (2023a), who carried out simulations of a similar system with slightly lower resolution of around 12.5 $M_\odot$. They find fluctuations of roughly two dex in the energy loading, while the mass loading is similar between the different codes they tested (GADGET, GIZMO, AREPO, and RAMSES). Moreover, they found that the biggest differences arise from Lagrangian (GADGET, GIZMO, and AREPO) versus Eulerian (Ramses) methods due to the higher spatial resolution in the Lagrangian codes. Our Lagrangian method predicts values for mass and energy loadings that are consistent with the ones that are put forward in the code comparison paper of Hu et al. (2023a). One potential issue with the energy loading is that it is quite sensitive to the exact velocity input. Since the energy outflow rate scales with the units of velocity cubed, it is not surprising that it fluctuates strongly between different numerical methods.

Finally, we note that Hu, Sternberg & van Dishoeck (2023b) carried out similar dwarf galaxy simulations with an active treatment for dust destruction and generation. They do find minor effects on outflow properties, but it would be interesting to investigate in future work how runaway stars could potentially contribute to dust enrichment of galactic outflows.

To summarize, our results indicate that even conservative modelling of runaway stars in galaxy simulations with a resolved treatment of the ISM and stellar feedback can have an impact on both the star formation history and the properties of large-scale SN-driven winds. This is most apparent in the energy outflow and energy loading factors, which we show in Figs 10 and 11, respectively. It is remarkable that the inclusion of runaway stars can boost the energy loading factor by as much as an order of magnitude, up to a value of $\sim$0.7 in the peak values. On average, we find an increase by roughly a factor of 5 in the model *WLM-runP* and a factor of 3 in the model *WLM-runM*. We note that previous work, such as from the TIGRESS suite (e.g. Kim & Ostriker 2015, 2018; Kim et al. 2020) or from the simulations of (e.g. Li, Bryan & Ostriker 2017), typically finds a value for the energy loading factor of around $\sim$0.1 for Milky Way-like conditions. Our results suggest that similarly high values of the energy loading might also be found in dwarf galaxies when runaway stars are included.

We can compare our results with two notable studies concerning runaway stars. One was presented by Andersson et al. (2020) and was carried out with the adaptive mesh refinement code Ramses (Teyssier 2002) in a global MW simulation. Another was carried out by Kim & Ostriker (2018) within the TIGRESS framework of local stratified environments with the grid code Athena. At face value, these studies

seem to disagree with one another, as Kim & Ostriker (2018) report that runaways have a very weak effect, while Andersson et al. (2020) report a significant boost in the wind outflow rates when runaway modelling is included. However, the comparison is tricky due to the different setup choices: Andersson et al. (2020) argue that their boost in outflow properties originates from the SNe that go off in lower-density gas outside the spiral arms, whereas this hypothesis is harder to test in simulations of stratified solar neighbourhood conditions. Furthermore, both studies use simulations that are evolved for a short amount of time compared to any global MW-scale. Our study with the Lagrangian code P-Gadget3 suggests that something in between these two studies might be true for the dwarf galaxy regime, as we do find that the outflow mass is boosted when runaway stars are included, similar to the findings of Andersson et al. (2020). However, the origin of this particular aspect of our simulation is likely the increase in star formation rate in the runaway models we simulated. For us, though, the largest impact is on the energetics of the outflows and not on the mass transport.[5]

A more direct comparison may be made with the recent follow-up study (Andersson et al. 2023), in which they simulated a system closer to the one described in the main paper of Smith et al. (2021) and in Hu et al. (2017) for their 'cmp' models. The dwarf in the (Andersson et al. 2023) system has a star formation rate that is a factor of 10 larger than in our runs; Andersson et al. (2023) used a 'resolved SN feedback prescription' along with subgrid stellar wind and also accounted for Type Ia SN explosions. The latter two aspects are unlikely to contribute much to the outflow driving itself but might be important for chemical enrichment. We note that Andersson et al. (2023) do not employ a treatment for PI radiation, which we believe might be the more important feedback channel at low metallicity compared to the stellar winds since emission line-driven stellar winds depend strongly on metallicity (e.g. Puls, Vink & Najarro 2008). The simulations of Andersson et al. (2023) report no effect on any of the galaxy properties they investigated (star formation history and outflow statistics) when adding runaway stars. They find higher values for the loading factors than our simulations do (by at least a dex), which is expected to some degree as the SN-only case is known to have higher star formation rates by a factor of a few and their system has a 10 times higher rate of star formation to begin with. It is interesting to note, though, that their outflow phase diagrams look very different from ours: they find much more hot gas in the outflow than we do. This is somewhat surprising since there is some consensus among nearly all codes that the hot gas mass in the outflows contributes only very little. Unfortunately, a more detailed exploration of this is beyond the scope of this work.

The comparison to the study of Kim & Ostriker (2018) is also interesting, since they sample from a Maxwell distribution as we do in our run *WLM-RunM*. However, they adopt a much larger velocity dispersion of 256 km s^{-1} in their Athena simulations. We adopted 32 km s^{-1} to mimic the more realistic and conservative approach of 'walkaway stars' (Renzo et al. 2019). Also, we note that they are operating their simulations in very different outflow regimes, as can be seen by comparing the shape of our Figs 8 and 9 to their results as shown in Kim et al. (2020), that is more appropriate for the solar neighbourhood (higher metallicity conditions). In our default simulations without runaway modelling, we do not find any hot wind in dwarf galaxies. While this is what is generally expected due to the less frequent SN breakouts, there is observational evidence for hot winds in low-mass galaxies (Heckman et al. 1995; Summers et al. 2003; Hartwell et al. 2004; Summers et al. 2004; Ott, Walter & Brinks 2005; McQuinn et al. 2018; McQuinn, van Zee & Skillman 2019), and our runaway star modelling supports this fact based on our findings of Fig. 9 where the runaway model *WLM-RunP* is producing a (very weak) hot wind and not just a warm wind as in the simulation *WLM-fiducial*. It will be interesting to see if these trends change in the new TIGRESS-ncr framework presented in Kim et al. (2022), because this is the setting that is the closest to ours when considering the implemented physics of non-equilibrium cooling and radiation.

Thus, our results seem to be somewhere in between the findings in Andersson et al. (2020) and Kim & Ostriker (2018), with runaways having a weaker impact than in the Milky Way simulations of Andersson et al. (2020) but a stronger impact than in the work of Kim & Ostriker (2018); they also do not have the negligible effect on the dwarf galaxy regime reported by Andersson et al. (2023). More numerical work needs to be done to determine the ultimate importance of runaway stars in galaxy evolution simulations and their role in outflow driving. However, in contrast with both studies, we find a significant increase in the appearance of high specific energy outflows; we note that while Kim & Ostriker (2018) are investigating energy loading as well, this is not put forward in Andersson et al. (2020). Nevertheless, we recommend that future resolved simulations include some treatment of runaways to capture this effect.

Finally, we can compare our result to the ones obtained in a cosmological context by Gutcke et al. (2022) who include 3 km s^{-1} velocity kicks on their stellar population and find that the mass loading is boosted by a factor of around 3.5, while the energy loading is only boosted by a factor of 1.7. While these numbers differ for us it is interesting that the effect of SNe repositioning seems to have an impact on the loading factors even in a more complex cosmological environment.

4.3 Model limitations

In this section, we briefly discuss some caveats and model limitations of our simulations. First, our two runaway models technically only represent a natal kick in a binary star formation scenario. However, we note that we only sample a single-star IMF that, strictly speaking, does not account for the fraction of the stars formed in binary or few-body systems. The latter would allow us to study more complex runaway scenarios such as the ejection of massive stars due to few-body interactions or the ejection of B stars in an OB binary due to supernova kicks when the O star explodes. However, this could be realized by adding a time delay to the kick, which is straightforward to implement in our code. It is not very likely that this would have a major impact on the conclusions of our study.

Additionally, we do not include an explicit pre-existing CGM around our dwarf galaxy, which could result in an overestimation of the boost in the outflow rates and loading factors. However, there are some arguments that support our picture even without the explicit inclusion of a low-density CGM around the dwarf. First, dwarfs have a very low virial temperature of $\sim 10^4$ K. In combination with the assumption of a very low density in the CGM compared to the galactic disc, it is rather unlikely that the CGM of dwarf galaxies is heavily supported by thermal pressure, which would work against the

[5] Andersson et al. (2020) do state that they find that runaway stars do not have any effect in dwarf galaxies, which they discuss very briefly without showing details. These appear to be very low-mass cosmological dwarf galaxy simulations taken from the EDGE sample (Agertz et al. 2020). Indeed, we find that if we apply the runaway modelling in lower-mass isolated discs, we also do not see a strong effect on any of the properties; this may be because these do not form a thin disc due to the strong impact of SN feedback. Hence our results are not necessarily in disagreement with what Andersson et al. (2020) report.

Table 2. Summary of the mean outflow diagnostics once the system has reached a quasiself-regulating state.

Name	SFR ($M_\odot$ yr^{-1})	$\dot{M}_{\rm out}$ ($M_\odot$ yr^{-1})	$\dot{M}_{\rm Z,out}$ ($M_\odot$ yr^{-1})	$\dot{p}_{\rm out}$ ($M_\odot$ km s^{-1} yr^{-1})	$\dot{E}_{\rm out}$ (10^{44} erg yr^{-1})
WLM-fiducial	0.00021	0.00632	8.26×10^{-6}	0.194	1.653
WLM-RunP	0.00029	0.00816	1.22×10^{-5}	0.291	7.915
WLM-RunM	0.00025	0.00757	1.07×10^{-5}	0.243	4.266
WLM-inplane	0.00022	0.00686	9.11×10^{-6}	0.200	2.973

Table 3. Summary of the mean loading factors once the system has reached a quasiself-regulating state.

Name	$\eta_{\rm M}^{\rm out}$	$\eta_{\rm Z}^{\rm out}$	$\eta_{\rm p}^{\rm out}$	$\eta_{\rm E}^{\rm out}$	$y_{\rm Z}^{\rm out}$
WLM-fiducial	28.0	1.3	2.93	0.010	1.089
WLM-RunP	29.0	1.60	3.31	0.051	1.23
WLM-RunM	31.2	1.61	3.42	0.036	1.15
WLM-inplane	30.9	1.35	3.00	0.014	1.089

thermal pressure provided by high altitude SNe due to the presence of runaway stars. Secondly, we note that the SN environmental density distributions in all runs are very similar and there is no excess of SNe in lower-density regions. This directly indicates that even above the disc scale height, the resolution still seems to be sufficient to model the evolution of individual SN remnants.

5 CONCLUSIONS AND OUTLOOK

5.1 Summary

We carried out high-resolution numerical simulations of isolated dwarf galaxies *with* and *without* a treatment for runaway stars to probe the effect of this process on galactic outflows and the related galaxy and ISM properties. We showed that the effect of runaway stars is mild with respect to the resulting structure of the multiphase ISM. Furthermore, we showed that there is an impact on the global star formation rate and the build-up of the total stellar mass of the system for all simulations that include runaway stars. While this results in very similar distributions for the PDFs of the environmental density where SNe explode, the run *WLM-RunP* shows a slight excess of SNe in lower-density environments that is beyond the intrinsic model scatter. However, the fact that all the models, including the run *WLM-inplane*, show similar SN density distributions is clear evidence that the main changes in global outflow evolution due to runaway stars are caused by the stars that explode at a higher altitude around the mid-plane. The fact that this trend remains for the weaker runaway model *WLM-RunM* indicates that runaway stars can heat the gas at the important boundary between the galactic disc and the CGM. This can be quantified by investigating the hot phase of the ISM in density-temperature phase space in the cases with and without runaway stars. Averaging over about half of the simulation run time, we find an excess in the mass of hot gas in the diffuse low-density ISM in the simulations with runaway stars.

In Fig. 10, we show the mass, metal, momentum, and energy outflow rates as a function of time. We find a slight boost in the overall mass outflow rate that is somewhat more dominant when only the metal mass is considered, providing the first evidence that runaway stars can lead to an excess of metals in the outflowing gas. The more dominant effect of the runaway stars can be seen in the momentum and energy outflow rates: the momentum outflow rate is boosted by at least a factor of two in the models *WLM-RunP* and *WLM-RunM*. The effect is even more dramatic for the energy outflow rate, which in the model *WLM-RunP* is boosted by almost one order of magnitude and in the model *WLM-RunM* increases by roughly a factor of 7. As this increase is not seen in the fiducial run *WLM-fiducial* or in the run *WLM-inplane* in which we apply the natal kicks only in the mid-plane of the galaxy, this provides clear evidence that runaway stars could contribute to the driving of high specific energy winds. We note that while these trends are also seen in the momentum and energy loading, they are somewhat reduced for the mass and metal outflow loading. There is a clear trend of stronger metal enrichment in the models that include the treatment of runaway stars. We summarize the mean outflow parameters after saturation in Table 2 and the mean outflow loading factors in Table 3.

The key findings of this paper can be summarized as follows:

(i) We find only a mild effect of runaway stars on the turbulent structure of the ISM as well as its phase structure.

(ii) The global star formation rate is increasing in the simulations with runaway stars, by around 20 per cent for the run *WLM-RunM* and 50 per cent for the run *WLM-RunM*.

(iii) The SN environmental density in the simulations with runaway stars is only weakly affected compared to the control run without runaway stars.

(iv) The inclusion of runaway stars can contribute to the build-up of the hot phase of the ISM and promote outflow launching due to an increase in the star formation rate.

(v) The inclusion of runaway stars can boost the mass outflow rate and metal outflow rate while keeping the mass outflow and metal outflow loading factors roughly constant compared to the fiducial run *WLM-fiducial*; this is caused by the increased star formation in the simulations with runaway stars.

(vi) Runaway stars can boost the momentum outflow rate by a factor of around 1.5, a trend that remains for the momentum outflow loading. We present evidence that this is primarily driven by SNe which explode at large heights above the disc (rather than simply in lower density regions within the disc), as these can more easily drive coherent outflows off the disc.

(vii) Runaway stars can boost the energy outflow rate by around a factor of 7 (*WLM-RunM*) to 10 (*WLM-RunP*) in the peaks and around 3 (*WLM-RunM*) to 5 (*WLM-RunP*) in the mean, a trend that remains for the momentum outflow loading. Therefore, they can potentially contribute to the origin of high specific energy winds in dwarf galaxies, as reported by some observational work (e.g. Heckman et al. 1995; Summers et al. 2003; Hartwell et al. 2004; Summers et al. 2004; Ott et al. 2005; McQuinn et al. 2018). However, we note that the higher values deduced from the run *WLM-RunP* should be interpreted as an upper limit for the effect.

5.2 Outlook and future work

We close by briefly discussing a few interesting ideas and implications for future work. While we find a rather weak impact of runaway stars on the mass outflow rate and, specifically, the outflow mass loading, runaway stars could have implications beyond what

is represented in our study. Recently, some groups have explored CR-driven winds (e.g. Pakmor et al. 2016; Buck et al. 2020; Hopkins et al. 2020, 2022a, b, 2021a, b, c; Hopkins 2023; Hopkins, Squire & Butsky 2022). In particular, Quataert, Thompson & Jiang (2022b) and Quataert, Jiang & Thompson (2022a) study in detail CR wind driving scenarios for CR streaming and CR diffusion. The outcome of this extensive analytic study is that winds driven by CR streaming require a significant Alfvén velocity v_A and thus magnetic-field strength. This is intrinsically hard to obtain in dwarf galaxies: the ISM turbulence is rather weak, due to low SN rates, which limits small-scale turbulent dynamo action. Furthermore, since dwarfs are often only weakly rotationally supported, there is no large-scale dynamo possible. On the other hand, the diffusion-driven winds require a large diffusion coefficient in order to obtain consistency with gamma-ray observations from pion decays that originate from CR protons, which puts rather tight constraints on the exact value of this coefficient. An interesting direction to explore in future work (both numerically and analytically) would be to constrain the effect of CRs seeded by runaway stars at or above the wind-launching scale; this could significantly contribute to outflows driven by CRs above the mid-plane. Hence, one could imagine runaway stars as an external boost for the CR diffusion coefficient. This could be explored with future simulations and improved analytic modelling.

ACKNOWLEDGEMENTS

We thank the anonymous referee for a very thorough report, which greatly improved this paper. UPS is supported by a Flatiron Research Fellowship (FRF) at the Center for Computational Astrophysics at the Flatiron Institute. The Flatiron Institute is supported by the Simons Foundation. RSS acknowledges support from the Simons Foundation. BB is grateful for funding support from the Simons Foundation, the Sloan Foundation, and the Packard Foundation. GLB acknowledges support from the NSF (AST-2108470, ACCESS), a NASA TCAN award, and the Simons Foundation through the Learning the Universe Simons Collaboration. UPS acknowledges useful discussions with Eric Andersson, Drummond Fielding, Chang-Goo Kim, Thorsten Naab, Eve Ostriker, and Romain Teyssier. UPS acknowledges the computing time provided by the Leibniz-Rechenzentrum (LRZ) in Garching on SuperMUC-NG under project number pn72bu, as well as the computing time on the c2pap-cluster in Garching under project number pr27mi, on which most the simulations presented here were carried out.

DATA AVAILABILITY STATEMENT

The data used in this article will be made available based on reasonable request to the corresponding author.

REFERENCES

Agertz O., Kravtsov A. V., Leitner S. N., Gnedin N. Y., 2013, ApJ, 770, 25
Agertz O. et al., 2020, MNRAS, 491, 1656
Andersson E. P., Agertz O., Renaud F., 2020, MNRAS, 494, 3328
Andersson E. P., Agertz O., Renaud F., Teyssier R., 2022, MNRAS, 521, 2196
Bakes E. L. O., Tielens A. G. G. M., 1994, ApJ, 427, 822
Banerjee S., Kroupa P., Oh S., 2012, ApJ, 746, 15
Bergin E. A., Hartmann L. W., Raymond J. C., Ballesteros-Paredes J., 2004, ApJ, 612, 921
Blaauw A., 1961, Bull. Astron. Inst. Netherlands, 15, 265
Buck T., Pfrommer C., Pakmor R., Grand R. J. J., Springel V., 2020, MNRAS, 497, 1712
Ceverino D., Klypin A., 2009, ApJ, 695, 292
Chieffi A., Limongi M., 2004, ApJ, 608, 405
Comerón F., Pasquali A., 2007, A&A, 467, L23
Dorigo Jones J., Oey M. S., Paggeot K., Castro N., Moe M., 2020, ApJ, 903, 43
Drew J. E., Monguió M., Wright N. J., 2021, MNRAS, 508, 4952
Eldridge J. J., Langer N., Tout C. A., 2011, MNRAS, 414, 3501
Emerick A., Bryan G. L., Mac Low M.-M., 2019, MNRAS, 482, 1304
Fielding D., Quataert E., Martizzi D., Faucher-Giguère C.-A., 2017, MNRAS, 470, L39
Forbes J. C., Krumholz M. R., Goldbaum N. J., Dekel A., 2016, Nature, 535, 523
Fujii M. S., Portegies Zwart S., 2011, Science, 334, 1380
Fujii M. S., Saitoh T. R., Hirai Y., Wang L., 2021, PASJ, 73, 1074
Gaburov E., Nitadori K., 2011, MNRAS, 414, 129
Gatto A. et al., 2017, MNRAS, 466, 1903
Genel S. et al., 2019, ApJ, 871, 21
Georgy C. et al., 2013, A&A, 558, A103
Gies D. R., 1987, ApJS, 64, 545
Girichidis P. et al., 2016, MNRAS, 456, 3432
Girichidis P., Pfrommer C., Pakmor R., Springel V., 2022, MNRAS, 510, 3917
Glover S. C. O., Clark P. C., 2012, MNRAS, 421, 9
Glover S. C. O., Mac Low M.-M., 2007, ApJS, 169, 239
Grond J. J., Woods R. M., Wadsley J. W., Couchman H. M. P., 2019, MNRAS, 485, 3681
Grudić M. Y., Guszejnov D., Offner S. S. R., Rosen A. L., Raju A. N., Faucher-Giguère C.-A., Hopkins P. F., 2022, MNRAS, 512, 216
Guedes J., Callegari S., Madau P., Mayer L., 2011, ApJ, 742, 76
Guszejnov D., Markey C., Offner S. S. R., Grudić M. Y., Faucher-Giguère C.-A., Rosen A. L., Hopkins P. F., 2022, MNRAS, 515, 167
Gutcke T. A., Pakmor R., Naab T., Springel V., 2021, MNRAS, 501, 5597
Gutcke T. A., Pakmor R., Naab T., Springel V., 2022, MNRAS, 513, 1372
Haid S., Walch S., Naab T., Seifried D., Mackey J., Gatto A., 2016, MNRAS, 460, 2962
Haid S., Walch S., Seifried D., Wünsch R., Dinnbier F., Naab T., 2018, MNRAS, 478, 4799
Hartwell J. M., Stevens I. R., Strickland D. K., Heckman T. M., Summers L. K., 2004, MNRAS, 348, 406
Heckman T. M., Dahlem M., Lehnert M. D., Fabbiano G., Gilmore D., Waller W. H., 1995, ApJ, 448, 98
Hirai Y., Fujii M. S., Saitoh T. R., 2021, PASJ, 73, 1036
Hirschmann M., Dolag K., Saro A., Bachmann L., Borgani S., Burkert A., 2014, MNRAS, 442, 2304
Hislop J. M., Naab T., Steinwandel U. P., Lahén N., Irodotou D., Johansson P. H., Walch S., 2022, MNRAS, 509, 5938
Hoogerwerf R., de Bruijne J. H. J., de Zeeuw P. T., 2000, ApJ, 544, L133
Hoogerwerf R., de Bruijne J. H. J., de Zeeuw P. T., 2001, A&A, 365, 49
Hopkins P. F., 2015, MNRAS, 450, 53
Hopkins P. F., 2023, MNRAS, 518, 5882
Hopkins P. F., Quataert E., Murray N., 2012, MNRAS, 421, 3522
Hopkins P. F., Kereš D., Oñorbe J., Faucher-Giguère C.-A., Quataert E., Murray N., Bullock J. S., 2014, MNRAS, 445, 581
Hopkins P. F. et al., 2018, MNRAS, 480, 800
Hopkins P. F. et al., 2020, MNRAS, 492, 3465
Hopkins P. F., Chan T. K., Ji S., Hummels C. B., Kereš D., Quataert E., Faucher-Giguère C.-A., 2021a, MNRAS, 501, 3640
Hopkins P. F., Chan T. K., Squire J., Quataert E., Ji S., Kereš D., Faucher-Giguère C.-A., 2021b, MNRAS, 501, 3663
Hopkins P. F., Squire J., Chan T. K., Quataert E., Ji S., Kereš D., Faucher-Giguère C.-A., 2021c, MNRAS, 501, 4184
Hopkins P. F., Butsky I. S., Panopoulou G. V., Ji S., Quataert E., Faucher-Giguere C.-A., Keres D., 2022a, MNRAS, 516, 3470
Hopkins P. F., Squire J., Butsky I. S., Ji S., 2022b, MNRAS, 517, 5413
Hopkins P. F., Squire J., Butsky I. S., 2022c, MNRAS, 509, 3779
Hu C.-Y., 2019, MNRAS, 483, 3363
Hu C.-Y., Naab T., Walch S., Moster B. P., Oser L., 2014, MNRAS, 443, 1173

Hu C.-Y., Naab T., Walch S., Glover S. C. O., Clark P. C., 2016, MNRAS, 458, 3528
Hu C.-Y., Naab T., Glover S. C. O., Walch S., Clark P. C., 2017, MNRAS, 471, 2151
Hu C.-Y., Sternberg A., van Dishoeck E. F., 2021, ApJ, 920, 44
Hu C.-Y., Schruba A., Sternberg A., van Dishoeck E. F., 2022, ApJ, 931, 28
Hu C.-Y. et al., 2023a, ApJ, 950, 132
Hu C.-Y., Sternberg A., van Dishoeck E. F., 2023b, ApJ, 952, 140
Keller B. W., Wadsley J. W., Wang L., Kruijssen J. M. D., 2019, MNRAS, 482, 2244
Kim C.-G., Ostriker E. C., 2015, ApJ, 802, 99
Kim C.-G., Ostriker E. C., 2018, ApJ, 853, 173
Kim C.-G., Ostriker E. C., Raileanu R., 2017, ApJ, 834, 25
Kim J.-G., Kim W.-T., Ostriker E. C., 2019, ApJ, 883, 102
Kim C.-G. et al., 2020, ApJ, 903, L34
Kim C.-G., Kim J.-G., Gong M., Ostriker E. C., 2023, ApJ, 946, 3
Kimm T., Cen R., 2014, ApJ, 788, 121
Kroupa P., 1995, MNRAS, 277, 1491
Lahén N., Naab T., Johansson P. H., Elmegreen B., Hu C.-Y., Walch S., Steinwand el U. P., Moster B. P., 2019a, ApJ, 891, 2
Lahén N., Naab T., Johansson P. H., Elmegreen B., Hu C.-Y., Walch S., 2019b, ApJ, 879, L18
Lancaster L., Ostriker E. C., Kim J.-G., Kim C.-G., 2021a, ApJ, 914, 89
Lancaster L., Ostriker E. C., Kim J.-G., Kim C.-G., 2021b, ApJ, 922, L3
Lejeune T., Cuisinier F., Buser R., 1997, A&AS, 125, 229
Lejeune T., Cuisinier F., Buser R., 1998, A&AS, 130, 65
Li M., Bryan G. L., Ostriker J. P., 2017, ApJ, 841, 101
Malkov O., Zinnecker H., 2001, MNRAS, 321, 149
Marinacci F., Pakmor R., Springel V., 2014, MNRAS, 437, 1750
Martizzi D., Faucher-Giguère C.-A., Quataert E., 2015, MNRAS, 450, 504
McQuinn K. B. W., Skillman E. D., Heilman T. N., Mitchell N. P., Kelley T., 2018, MNRAS, 477, 3164
McQuinn K. B. W., van Zee L., Skillman E. D., 2019, ApJ, 886, 74
Naab T., Ostriker J. P., 2017, ARA&A, 55, 59
Nelson D. et al., 2018, MNRAS, 475, 624
Nelson D. et al., 2019, MNRAS, 490, 3234
Oh S., Kroupa P., 2016, A&A, 590, A107
Orr M. E., Fielding D. B., Hayward C. C., Burkhart B., 2022a, ApJ, 924, L28
Orr M. E., Fielding D. B., Hayward C. C., Burkhart B., 2022b, ApJ, 932, 88
Ott J., Walter F., Brinks E., 2005, MNRAS, 358, 1453
Pakmor R., Pfrommer C., Simpson C. M., Springel V., 2016, ApJ, 824, L30
Perets H. B., Šubr L., 2012, ApJ, 751, 133
Pillepich A. et al., 2018, MNRAS, 473, 4077
Poveda A., Ruiz J., Allen C., 1967, Bol. Obs. Tonantzintla y Tacubaya, 4, 86
Puls J., Vink J. S., Najarro F., 2008, A&AR, 16, 209
Quataert E., Jiang F., Thompson T. A., 2022a, MNRAS, 510, 920
Quataert E., Thompson T. A., Jiang Y.-F., 2022b, MNRAS, 510, 1184
Rantala A., Pihajoki P., Johansson P. H., Naab T., Lahén N., Sawala T., 2017, ApJ, 840, 53
Rantala A., Pihajoki P., Mannerkoski M., Johansson P. H., Naab T., 2020, MNRAS, 492, 4131
Renzo M. et al., 2019, A&A, 624, A66
Schaye J. et al., 2015, MNRAS, 446, 521
Silva M. D. V., Napiwotzki R., 2011, MNRAS, 411, 2596
Smith M. C., Bryan G. L., Somerville R. S., Hu C.-Y., Teyssier R., Burkhart B., Hernquist L., 2021, MNRAS, 506, 3882
Somerville R. S., Davé R., 2015, ARA&A, 53, 51
Spitzer L., 1987, Dynamical Evolution of Globular Clusters. Princeton Univ. Press, Princeton
Springel V., 2005, MNRAS, 364, 1105
Springel V., Di Matteo T., Hernquist L., 2005, MNRAS, 361, 776
Steinwandel U. P., Moster B. P., Naab T., Hu C.-Y., Walch S., 2020, MNRAS, 495, 1035
Steinwandel U. P., Kim C.-G., Bryan G. L., Ostriker E. C., Somerville R. S., Fielding D. B., 2022, preprint (arXiv:2212.03898)
Stone R. C., 1991, AJ, 102, 333
Summers L. K., Stevens I. R., Strickland D. K., Heckman T. M., 2003, MNRAS, 342, 690
Summers L. K., Stevens I. R., Strickland D. K., Heckman T. M., 2004, MNRAS, 351, 1
Teyssier R., 2002, A&A, 385, 337
Vogelsberger M. et al., 2014, MNRAS, 444, 1518
Walch S. et al., 2015, MNRAS, 454, 238
Westera P., Lejeune T., Buser R., Cuisinier F., Bruzual G., 2002, A&A, 381, 524
Wolfire M. G., McKee C. F., Hollenbach D., Tielens A. G. G. M., 2003, ApJ, 587, 278

This paper has been typeset from a TEX/LATEX file prepared by the author.